INSTITUTE OF PLASMA PHYSICS

NAGOYA UNIVERSITY

Collisionless Tearing Instabilities

I. Katanuma and T. Kamimura

IPPJ- 370 January 1979

RESEARCH REPORT

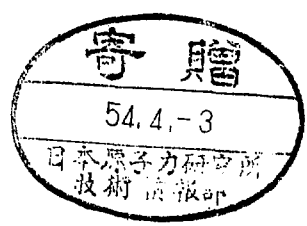

NAGOYA, JAPAN

Collisionless Tearing Instabilities

I. Katanuma and T. Kamimura

IPPJ- 370 January 1979

Further communication about this report is to be sent to the Research Information Center, Institute of Plasma Physics, Nagoya University, Nagoya 464, Japan.

Abstract

Collisionless tearing modes and the enhanced transport associated with this instability are investigated theoretically and by using a two-and-one-half dimensional particle simulation code in a slab geometry. The effects of electrostatic fields on the instability are also considered. The initial current is found to diffuse along the perturbed magnetic field lines with the observed diffusion coefficient in good agreement with the theoretical prediction. Electrostatic effects have a tendency to enhance the tearing mode growth rate. The growth of the mode is observed to divide into three phases. In multi-mode tearing, a combination of magnetic islands is observed.

§1 Introduction

Tearing modes are believed to play an important role in both tokamak discharges and space plasmas. In a tokamak discharge, a tearing mode is experimentally[1] observed to precede the disruptive instability. High m number tearing modes (where m is the poloidal mode number) may break up the magnetic surfaces and enhance particle and energy transport, even though their amplitude is small.[2]

In the original investigations of the linear phase,[3] the plasma was assumed to be a resistive medium, and tearing modes were described with collisional MHD equations. Recent vigorous theoretical and numerical studies[4-8] to understand the disruptive instability or tearing mode have also mainly been based on the collisional MHD equations. However, recently some authors[9,10] extended the calculation to the collisionless regime by including electron inertia. Recently, Hazeltine, et al.[11] and Drake and Lee [12] unified these calculations by carrying out a kinetic theory with a Fokker-Plank collision operator. Especially Drake and Lee[12] found that tearing modes in present-day high temperature tokamak discharges occur in the semi-collisional regime, in which the width of the singular layer around $\underset{\sim}{k}\cdot\underset{\sim}{B}_0 = 0$ is limited by electron thermal motion along the magnetic field. In this regime the collisional MHD equations do not reasonably describe the phenomena. Also, the width of the singular layer can easily become smaller than the ion gyro-radius in present-day tokamak discharges, where $s \sim 10^2$ to 10^3 (s is the magnetic Reynolds number). This, too, is beyond the MHD description.

Collisionless tearing modes may not be a possible mechanism for the anomalous plasma transport or the sawtooth oscillation in current tokamak discharges because of its small growth compared with the electron-electron or the electron-ion collision frequency. In future tokamak discharges or in fusion reactors, however, collisionless tearing modes may take the place of semi-collisional ones. Furthermore, the major disruption may be collisionless even in present tokamaks due to its large growth rate, even though its mechanism is unknown. It is, therefore, necessary to investigate the tearing instability in the collisionless regime.

In a space plasma, collisionless tearing modes are believed to be one of the most effective mechanisms for magnetic field line reconnection.[13,14] This is particularly true for the Earth's magnetospheric tail where the particle mean-free-path is anomalously large.

In this paper we investigate the collisionless tearing mode both analytically and with computer simulations in slab geometry. Referring to Fig.1, a slab of current j_z of half width a which is uniform in the y-z plane moves along a large B_z field. A self-consistent $B_y(x)$ field ($|B_y| << |B_z|$), which reverses direction across the current sheet at $x = \frac{1}{2}L_x$, is produced by the current. We impose periodic boundary conditions in the y direction and conducting walls at both x boundaries. Sec. 2 obtains the linear dispersion relation applicable to both inner and outer regions using a drift kinetic theory and also gives a quasi-linear theory which describes the decay of the initial current layer. To date,

in the collisionless regime, electrostatic effects have been neglected.[12,13] However, it is also shown in Sec.2 that the electrostatic effects have a tendency to spread out the width of a magnetic island and to raise the tearing growth rate. Sec.3 describes a two-and-one-half dimensional magnetostatic particle model in which the compressional mode of the axial magnetic field is neglected. The simulation results are presented in Sec.4. The results agree well with the theoretical predictions obtained in Sec.2. The nonlinear saturation mechanism is observed to be the spreading out of the initial current layer quasi-linearly into the stable state. During the transition between the linear and nonlinear phases, a quasi-stable state is also observed which has been predicted by Drake and Lee.[15] The nonlinear evolution of the width of magnetic island is proportional to time. This situation is called the Rutherford phase[16] in the collisional regime. We also find that when several modes are unstable as to tearing mode, two magnetic islands will unite into one large island.

§2 Theory

In this system shown in Fig.1, the current sheet is stable in absence of non-ideal magnetohydrodynamic effects such as inertia or resistivity. In the collisionless case, however, inertia makes the system unstable and relaxes it to a lower magnetic energy state. Magnetic field lines slip with respect to the plasma near the central layer (around $x \simeq L_x/2$), producing an induced electric field $\underset{\sim}{E}$ which accelerates electrons along

the magnetic field. The perturbed current $\underset{\sim}{J}$ is then localized near the central layer.

We now treat the colisionless tearing mode nonlocally, subject to the following several assumptions[12]:

1. The perturbed current $\underset{\sim}{J}$ which is produced by the induced electric field is primarily along the axial magnetic field (i.e. along the Z direction). This corresponds to neglecting the compressional mode of the magnetic field and is a good approximation for a low β plasma.

2. The response of the electrons to the induced electric field and the perturbed magnetic field is much larger than that of the ions. Therefore we consider only the electron motion in this section.

3. In the outer region, the induced scalar potential $\tilde{\phi}$ is negligible while the relation $k_{\parallel}\tilde{\phi}/(\omega\tilde{A}_z/c) \ll 1$ holds in the inner region. Here $k_{\parallel}$ is the component of the wave vector along the magnetic field and A_z the z-component of the perturbed vector potential. The induced scalar potential, therefore, will be neglected in all regions in the collisionless case. In the last part of this section, however, we point out the effects of the potential cannot be neglected in some cases.

The initial equilibrium is basically described in Fig.1. A plane plasma slab is immersed in a sheared magnetic field

$$\underset{\sim}{B}_0 = B_z\hat{e}_z + B_y(x)\hat{e}_y \quad , \quad |B_z| \gg |B_y| \quad . \qquad (1)$$

The number and current density vary only in the x direction. The electron distribution in this configuration can be written in the form[17]

$$f_0(x,v^2,P_z)=\left(\frac{m_e}{2\pi T_e}\right)^{3/2}\exp-\frac{1}{T_e}\left\{\frac{1}{2}m_e v^2+\frac{1}{2m_e}[P_z-m_e v_{0z}(x)]^2-\frac{P_z^2}{2m_e}\right\} \quad . \tag{2}$$

where m_e and T_e are electron mass and temperature; v_{oz} is the electron drift velocity along the axial magnetic field; P_z is the Z component of the canonical momentum,

$$P_z = m_e v_z - eA_z/c \quad ; \tag{3}$$

and A_z is the Z component of the equilibrium vector potnetial. Writing $n(x)=n_o\exp-\{\frac{e}{T_e c} v_{oz} A_z\}/\int_0^{L_x} dx \exp -\{\frac{e}{T_e c} v_{oz} A_z\}$ gives the equilibrium density balanced by magnetic forces:

$$f_0(x,v^2,v_z)= \left(\frac{m_e}{2\pi T_e}\right)^{3/2}\frac{n(x)}{n_0} \exp - \frac{1}{T_e}\left\{\frac{1}{2} m_e v^2 - m_e v_z v_{oz}(x) + \frac{1}{2} m_e v_{oz}^2(x)\right\} . \tag{4}$$

We use this electron equilibrium distribution function in the following analysis.

2.1 Linear theory

The width of the singular layer of the tearing mode is much larger than the mean electron Larmor radius, and in the case of pure tearing modes (i.e., no density and temperature gradients), the characteristic frequency is nearly equal to zero, and this is much smaller than the electron gyro-frequency. We can use drift-kinetic equations to describe the electron motion in this case. The first-order electron distribution becomes

$$\left(\frac{\partial}{\partial t} + v_{\parallel}\frac{B_y}{B_z}\frac{\partial}{\partial y}\right)\tilde{f} = -v_{\parallel}\frac{\tilde{B}_x}{B_z}\frac{\partial}{\partial x}f_0 + \frac{e}{m_e}\tilde{E}_{\parallel}\frac{\partial}{\partial v_{\parallel}} f_0 \quad . \tag{5}$$

where the subscript $_{\parallel}$ refers to the component of the vector along B_0. Eq.(5), therefore, contains only the electron response to the parallel electric field. The perturbed fields are represented by a vector potential as

$$\tilde{\underset{\sim}{B}} = \nabla \times \tilde{A}_z \, \hat{e}_z \, , \tag{6}$$

$$\tilde{E}_{\parallel} = - \frac{1}{c} \frac{\partial}{\partial t} \tilde{A}_z \, . \tag{7}$$

$\tilde{A}_z$ is driven by the perturbed plasma current:

$$\Delta \tilde{A}_z = - \frac{4\pi n_0 e}{c} \int d\underset{\sim}{v} \, v_{\parallel} \, \tilde{f} \quad , \tag{8}$$

where we may neglect the displacement current for low frequency modes. The x and y components of the vector potential are assumed to be small compared with the z component in the approximation that the perturbed plasma currents are primarily along the z direction. Now supposing the perturbed quantities take of the form $\tilde{A}_z(\underset{\sim}{r}, t) = \tilde{A}_z(x) \exp[i(k_y y + k_z z - \omega t]$, Eqs.(5), (6) and (7) yield

$$\tilde{f} = \frac{1}{\omega - k_{\parallel} v_{\parallel}} \{ \frac{e\omega}{T_e c} [v_{\parallel} - v_{oz}] + \frac{m_e k_y}{B_z T_e} \, v_{\parallel} [v_{\parallel} - v_{oz}] \frac{\partial}{\partial x} \, v_{oz} \} \tilde{A}_z \, . \tag{9}$$

where $k_{\parallel} = \underset{\sim}{k} \cdot \underset{\sim}{B}_0 / B_0$, and the diamagnetic drift term associated with the density gradient is neglected. Inserting Eq.(9) into Eq.(8) we finally obtain

$$\left(\frac{\partial^2}{\partial x^2} - k^2 \right) \tilde{A}_z = \frac{1}{c^2 \lambda_{De}^2} \{ \omega [\langle\langle v_{\parallel}^{\ell} \rangle\rangle - v_{oz} \langle\langle v_{\parallel} \rangle\rangle]$$

$$- \frac{k_y}{\omega_{ce}} [\langle\langle v_{\parallel}^{3} \rangle\rangle - v_{oz} \langle\langle v_{\parallel}^{2} \rangle\rangle] \frac{\partial}{\partial x} \, v_{oz} \} \tilde{A}_z \, , \tag{10}$$

$$\langle\langle v_{\parallel}^{\,n} \rangle\rangle = \int d\underset{\sim}{v} \frac{v_{\parallel}^{\,n}}{\omega - k_{\parallel} v_{\parallel}} f_0 \quad . \tag{11}$$

where $k^2 = k_y^2 + k_z^2$, $\lambda_{De} = (T_e/4\pi n_0 e^2)^{1/2}$ is the electron Debye length, and $\omega_{ce} = eB_z/m_e c$ is the electron gyro-frequency in the axial magnetic field. The first two terms on the right side of Eq.(10) are important in the singular layer where electrons are accelerated by the induced electric field and where the initial current peaks. The last two terms on the right side are sensitive to the initial current profile and the geometry and determine whether the plasma is stable against tearing modes.

We now consider what condition reduces Eq.(10) to the known dispersion relation. First, consider Eq.(10) in the singular layer, where the current density is nearly uniform. Assuming $\partial^2/\partial x^2 \gg k^2$, and neglecting the parallel electron drift velocity compared with the electron thermal velocity, Eq.(10) reduces to

$$\frac{\partial^2}{\partial x^2} \tilde{A}_z = k_0^{\,2} \tilde{A}_z \, s^2 \frac{d}{ds} Z(s) \quad . \tag{12}$$

where $k_0^{-1} = c/\omega_{pe}$ is the collisionless skin depth, $s = \omega/k_{\parallel} v_e$, $v_e = (2T_e/m_e)^{1/2}$, and $Z(s)$ is the plasma dispersion function.[18] The discontinuity in the outer solutions is simply represented by

$$\Delta' = [\frac{\partial}{\partial x} \tilde{A}_z(L_x/2+\lambda) - \frac{\partial}{\partial x} \tilde{A}_z(L_x/2-\lambda)]/\tilde{A}_z(L_x/2) \quad . \tag{13}$$

Here, λ stands for the width of the singular layer, limited by the electron thermal velocity according to the relation $k_{\parallel}(L_x/2+\lambda)v_e = \gamma$. ($\gamma$ is the linear growth rate of the tearing mode.) We integrate Eq.(12) over the layer assuming $k_{\parallel} = (x-L_x/2)k_y/\ell_s$ and

the perturbed vector potential $\tilde{A}_z$ to the constant[3,12] and obtain

$$\gamma = k_y v_e \Delta'/2k_0^2 \ell_s \sqrt{\pi} \quad . \tag{14}$$

where ℓ_s is the magnetic shear length around $x=L_s/2$. This growth rate γ coincides with the result derived by Drake and Lee.[12]

On the other hand, $k_{\parallel} v_e$ is greater than γ in the outer region, so that the electrons are not accelerated but rather feel an AC acceleration by the parallel elelectric field. Therefore ω can be neglected in this region, as well as the parallel electron drift velocity. Considering of the terms in the current shear in Eq.(10) gives

$$\frac{\partial^2}{\partial x^2} \tilde{A}_z = k^2 \tilde{A}_z + [\frac{\partial^2}{\partial x^2} (\underset{\sim}{k}\cdot\underset{\sim}{B})] \tilde{A}_z/(\underset{\sim}{k}\cdot\underset{\sim}{B}_0) \quad . \tag{15}$$

Solving of Eq.(15) with appropriate boundary conditions produces a discontinuity represented by Δ' in the slope of $\tilde{A}_z$ across the current layer. Eq.(15) coincides with the ideal MHD equation applied to the outer region which was derived by Furth, et al.[3]

Now we solve Eq.(10) numerically with the boudary conditions, $A_z=0$ at $x=0$ and $x=L_x$. A calculation is carried out with a shooting method. The physical parameters used here are $c/(T_e/m_e)^{1/2}= 10$, $\omega_{ce}/\omega_{pe} = 1.5$, $L_x = 64\lambda_{De}$, $k_y = 2\pi/64\lambda_{De}$, and $k_z=0$. The current profile is gaussian: $J_z(x) = j_{oz}\exp[-(\ell n2)(x-L_x/2)^2/a^2]$, $j_{oz}=en_0(T_e/m_e)^{1/2}$. The numerical results are illustrated in Fig.2. There are an upper limit and

a lower limit for $k_y a$ for stability, as shown in Fig.2a. The maximum growth rate is at $k_y a \simeq 0.3$. Fig.2b shows the vector potential $\tilde{A}_z$ eigenfunction for the case $k_y a = 0.5$ in which $\tilde{A}_z$ is found to be almost even function about $x=L_x/2$, so we present the profile in a half range ($L_x/2$ to L_x). These features closely resemble those of the collisional case.[19]

2.2 Quasi-linear theory

Quasi-linear effects are important for plasma diffusion and may be responsible for the saturation of the tearing instability. The quasi-linear equation for the electron distribution function in the drift approximation can be written as

$$\frac{\partial}{\partial t} f_0 = \sum_k \left[\frac{e}{m_e} \tilde{E}_{k\parallel}^* \frac{\partial}{\partial v_\parallel} - v_\parallel \frac{\tilde{B}_{kx}^*}{B_z} \frac{\partial}{\partial x}\right] \tilde{f}_k \quad . \tag{16}$$

Using Eq.(5) we can obtain the diffusion equation for the distribution function in phase space. For a pure tearing mode, however, the electrons resonant with the wave cover almost the entire region in velocity space. We, therefore, consider configuration space diffusion.

It is particularly interesting to understand the current relaxation in a current sheet. The integration over all velocity space of the product of Eq.(16) and the Z component of velocity, using Eq.(5), yields

$$\frac{\partial}{\partial t} j_z = i\sum_k \Big\{ \frac{e}{cB_z T_e} \tilde{E}_{k\parallel}^* \tilde{B}_{kx} [\langle\langle v_\parallel^2 \rangle\rangle - v_{oz} \langle\langle v_\parallel \rangle\rangle] \frac{\partial}{\partial x} j_z$$

$$+ \frac{n_0 e^3}{m_e c^2 T_e} \tilde{E}_{k\parallel}^* \tilde{E}_{k\parallel} [\langle\langle v_\parallel \rangle\rangle - v_{oz} \langle\langle 1 \rangle\rangle]$$

$$+ \frac{m_e}{B_z T_e} \tilde{B}_{kx}^* \frac{\partial}{\partial x} \frac{\tilde{B}_{kx}}{B_z} [\langle\langle v_\parallel^4 \rangle\rangle - v_{ox} \langle\langle v_\parallel^3 \rangle\rangle] \frac{\partial}{\partial x} j_z$$

$$+ \frac{n_0 e^2}{cB_0 T_e} \tilde{B}_{kx}^{*} \frac{\partial}{\partial x} \tilde{E}_{k\parallel} [\langle\langle v_\parallel^3 \rangle\rangle - v_{ox} \langle\langle v_\parallel^2 \rangle\rangle] \} \qquad (17)$$

where $j_z = -en_0 \int dv\, v_z f_0$. If we focus on modes with $R_e\omega_k = 0$, $I_m\omega_k = \gamma_k$, and neglect the higer order terms of γ_k, Eq.(17) reduces to

$$\frac{\partial}{\partial t} j_z = \sum_k \frac{\tilde{B}_{kx}^{*}}{B_z} \frac{\partial}{\partial x} \{ \frac{\tilde{B}_{kx}}{B_z} \frac{\gamma_k}{k_\parallel^2} \frac{\partial}{\partial x} j_z \} - \frac{\omega_{pe}}{4\pi c} \sum_k \frac{\tilde{B}_{kx}^{*}}{B_z} \frac{\partial}{\partial x} \frac{\tilde{E}_{k\parallel}}{k_\parallel}. \qquad (18)$$

The first term represents the current diffusion along the perturbed magnetic field lines. The last term describes the growth of the total current corresponding to the change in the electron energy.

The current diffusion term in Eq.(18) can be interpreted as follows. The diffusion coefficient D_j corresponding to resonant electrons in the x direction is estimated as

$$D_j = \sum_k \langle (v_\parallel \frac{\tilde{B}_{kx}}{B_z})^2 \rangle \tau_k \quad . \qquad (19)$$

Here τ_k is a correlation time for each k mode. Noting that the relation $k_\parallel v_\parallel \simeq \gamma_k$ holds on each side of the singular layer and estimating τ_k as the wave life time $1/\gamma_k$, we find that D_j becomes

$$D_j = \sum_k \frac{|\tilde{B}_{kx}|^2}{B_z^2} \frac{\gamma_k}{k_\parallel^2} \quad . \qquad (20)$$

Therefore the current diffusion coefficient is given by Eq.(20) as long as the current diffusion may be considered to be the diffusion of the current-carrying electrons.

This current diffusion due to quasi-linear effects decreases

the anisotropy of the distribution function given in Eq.(4) which is the essential source of the tearing instability. Moreover this diffusion carries the plasma information away from the layer, which leads to anomalous plasma transport.

2.3 Electrostatic effects

The acceleration of resonant electrons by a tearing mode forms a charge density gradient between the magnetic field lines. The resultant electrostatic fields cause a current distortion through the $\underset{\sim}{E} \times \underset{\sim}{B}$ drift of electrons. We now estimate the growth rate of a pure tearing mode in the singular layer including this effect, using the heuristic argument presented by Drake and Lee.[12)]

The perturbed electron drift velocity, in response to the parallel electric field defined in Eq.(7), is given by

$$\tilde{v}_z = e \tilde{A}_z / m_e c \ . \tag{21}$$

This drift velocity yields the perturbed electron density. Using the continuity equation, we obtain

$$\tilde{n} = -ik_{\parallel} e n_0 \tilde{A}_z / \gamma_L m_e c \ . \tag{22}$$

where γ_L is the linear growth rate without electrostatic effects. This perturbed density produces the scalar potential $\tilde{\phi}_k$ through the Poisson equation,

$$\frac{\partial^2}{\partial x^2} \tilde{\phi}_k = - ik_{\parallel} \omega_{pe}^2 \tilde{A}_z / \gamma_L c \ . \tag{23}$$

Where we assume $k^2 << \partial^2/\partial x^2$. The electrostatic field along the magnetic field lines produced by the scalar potential has

a tendency to cancel the induced electric field. This effect, however, is neglected according to the third of the assumptions stated previously. Instead, we take into account the electrostatic field across the magnetic field lines.

Now let us consider the electron motion near an x-type neutral point as shown in Fig.3. The electrons near the point flow in the shaded region in Fig.3 by $[\underset{\sim}{E} \times \underset{\sim}{B}]_x$ drift carrying current $j_z(L_x/2+\lambda)$, whereas the electrons in the shaded region flow out from there by $[\underset{\sim}{E} \times \underset{\sim}{B}]_y$ drift carrying current $j_z(L_x/2)$. This motion, therefore, causes an additional perturbed current in the region. (The same argument holds near an O-type neutral point.) The additional perturbed current j_{zef} is estimated to be

$$\tilde{j}_{zef} \simeq -i\frac{k_y c}{B_z \gamma_L}[j_z(L_x/2+\lambda) - j_z(L_x/2)]\frac{\partial}{\partial x}\tilde{\phi}_k \quad . \tag{24}$$

where $\underset{\sim}{B}_0 \simeq B_z \hat{e}_z$ is assumed. We suppose $\partial\phi_k/\partial x \simeq$ const. and $\tilde{A}_z \simeq$ const. in the singular layer. Using Eq.(23), we get

$$\tilde{j}_{zef} \simeq -\frac{k_y^2 \omega_{pe}^2 \lambda^2}{B_z \gamma_L^2 \ell_s}[j_z(L_x/2+\lambda) - j_z(L_x/2)]\tilde{A}_z. \tag{25}$$

On the other hand, the perturbed current j_z produced by the induced electric field is obtained from Eq.(21),

$$\tilde{j}_z = -\frac{n_0 e^2}{m_e c}\tilde{A}_z \quad . \tag{26}$$

The perturbed current in Eq.(26) leads to tearing, which produces the discontinuity in $\partial\tilde{A}_z/\partial x$ across the sigular layer that is usually considered in most theoretical treatments. The scheme to find the linear growth rate γ_L with the heuristic

derivation is the same as that presented in section 2.1. Namely, using Eq.(13), Ampere's law is modified to be

$$\Delta' \tilde{A}_z = - (4\pi/c)\lambda \tilde{j}_z \quad . \tag{27}$$

Then in assuming that we may ignore the electrostatic effects, we find that the linear growth rate becomes

$$\gamma_L \simeq k_y v_e \Delta'/k_0{}^2 \ell_s \quad . \tag{28}$$

where $k_{\parallel}(L_x+2/\lambda)v_e = k_y \lambda v_e/\ell_s \simeq \gamma_L$ is assumed. This growth rate was obtained also by Drake and Lee.[12]

It is interesting to compare $\tilde{j}_{zef}$ with the $\tilde{j}_z$ of Eq.(26) before calculating the growth rate γ_{ef} which includes electrostatic effects. The current $\tilde{j}_z$ corresponds to the current peaking around the x-type neutral point. This shows that energy is exchanged between resonant electrons and the magnetic field. However, $\tilde{j}_{zef}$ appears as a result of the current layer being distorted by the current-carrying electron $\tilde{E} \times \tilde{B}$ drifts, in which there is no energy exchange. For the usual current profile, $|j_z(L_x/2)| > |j_z(L_x 2+\lambda)|$, $\tilde{j}_{zef}$ is of opposite sign to $\tilde{j}_z$, which shows that, for the case when $|\tilde{j}_z| > |\tilde{j}_{zef}|$, the current peaks at the x-type neutral point, whereas if, $|\tilde{j}_z| < |\tilde{j}_{zef}|$, the current tears at the point.

We now calculate the growth rate including electrostatic effects. The total perturbed current $\tilde{j}_{ztot}$ is

$$\tilde{j}_{ztot} = \tilde{j}_z + \tilde{j}_{zef}$$

$$= - \frac{n_0 e^2}{m_e c} \tilde{A}_z + \frac{k_y{}^2 c \omega_{pe}{}^2 \lambda^2}{4\pi \gamma_L{}^2 \ell_s{}^2} [1 - j_z(L_x/2+\lambda)/j_z(L_x/2)] \tilde{A}_z \quad . \tag{29}$$

Inserting Eq.(29) into Eq.(27), we have the dispersion relation:

$$\Delta' = k_0^2\lambda - \frac{k_0^2 c^2 k_y^2}{\gamma_L^2 \ell_s^2}\lambda^3 [1-j_z(L_x/2+\lambda)/j_z(L_x/2)] . \qquad (30)$$

Noting that $k_y \lambda v_e/\ell_s \simeq \gamma_{ef}$, the growth rate is given by

$$\gamma_{ef} \simeq \gamma_L\{1+(\frac{c\,\gamma_{ef}}{v_e\gamma_L})^2[1 - j_z(L_x/2+\lambda)/j_z(L_x/2)]\} \quad . \qquad (31)$$

The last two terms on the right side describe the contribution of electrostatic effects to the growth rate. When $|j_z(L_x/2)| > |j_z(L_x/2+\lambda)|$, electrostatic effects always increase the growth rate.

It is important to note that magnetic reconnection may not occur in collisionless tearing mode as long as only electron acceleration by the induced electric field is considered. However if we consider also electrostatic effects, reconnection may occur because these effects play the role of current dissipation at an x-type neutral point.

§3 The simulation model

In particle computer simulation, the magnetostatic model[20,21] is a powerful tool to investigate low frequency plasma phenomena with magnetic field perturbations, such as tearing modes. For such phenomena, when the wave vector is nearly perpendicular to the external axial magnetic field, the compressional component of the magnetic field perturbation can be neglected. In the magnetostatic model, the displacement current is ignored, and hence high frequency modes due to radiation are eliminated.

The equations for this model are:

$$\nabla \cdot \underset{\sim}{E}_L = 4\pi\rho \quad , \tag{32}$$

$$\nabla \times \underset{\sim}{B} = \frac{4\pi}{c} j_{zT}\, \hat{e}_z \quad , \tag{33}$$

$$\nabla \times E_{zT}\, \hat{e}_z = -\frac{1}{c}\frac{\partial}{\partial t}\underset{\sim}{B} \quad . \tag{34}$$

where subscripts L and T denote longitudinal ($\nabla \times A_L = 0$) and transverse ($\nabla \cdot A_T = 0$) components, respectively. ρ and j_{zT} are given by summing over all simulation particles:

$$\rho(\underset{\sim}{r}) = \sum_j q_j\, S(\underset{\sim}{r} - \underset{\sim}{r}_j) \quad , \tag{35}$$

$$j_{zT}(\underset{\sim}{r}) = [\sum_j q_j\, v_{zj}\, S(\underset{\sim}{r} - \underset{\sim}{r}_j)]_T \quad . \tag{36}$$

where

$$S(\underset{\sim}{r}) = \frac{1}{2\pi a_p^{\,2}} \exp -\{\frac{1}{2} r^2/a_p^{\,2}\} \quad , \tag{37}$$

simulation particles are assumed to have a gaussian form factor for the finite-size simulation particles.[22] In order to calculate the field quantities efficiently, a spatial grid is introduced. The sums appearing in Eqs.(35) and (36) are performed by the technique known as the subtracted dipole scheme (SUDS).[23]

It is well known that a straightforward integration in time of Eqs.(32), (33) and (34) leads to numerical instability. Hence Eq.(34) is equivalently modified to be[20,21]

$$\Delta E_{zT} = \frac{4\pi}{c^2}[\sum_j \frac{q_j^{\,2}}{m_j} S(\underset{\sim}{r}-\underset{\sim}{r}_j) \int S(\underset{\sim}{r}'-\underset{\sim}{r}_j)\, E_{zT}(\underset{\sim}{r}')\, d\underset{\sim}{r}']_T$$

$$+ \frac{4\pi}{c^2}\left[\sum_j \frac{q_j^2}{m_j} S(\underset{\sim}{r}-\underset{\sim}{r}_j)\int S(\underset{\sim}{r}'-\underset{\sim}{r}_j)\left[\frac{\underset{\sim}{v}_j}{c}\times\underset{\sim}{B}(\underset{\sim}{r}')\right]_z d\underset{\sim}{r}'\right.$$

$$\left. - q_j v_{zj} (\underset{\sim}{v}_j \cdot \nabla) S(\underset{\sim}{r} - \underset{\sim}{r}_j)\right]_T \quad . \tag{38}$$

The equations of motion for the particles are

$$m_j \frac{d}{dt}\underset{\sim}{v}_j = q_j \int S(\underset{\sim}{r}_j-\underset{\sim}{r}')\left[\underset{\sim}{E}_L(\underset{\sim}{r}')+E_{Tz}(\underset{\sim}{r}')\hat{e}_z+\frac{\underset{\sim}{v}_j}{c}\times B(\underset{\sim}{r}')\right]d\underset{\sim}{r}' \quad . \tag{39}$$

and are integrated in time by the usual leap-frog scheme. Both ions and electrons are included. The geometry in the simulation is the same as that shown in Fig.1. The system is periodic in the y direction and is bounded by two conducting walls at x=0 and $x=L_x$ in the x direction. We assume that there is no spatial change in the z direction. Paricles have three components of velocity (v_x, v_y, v_z), which is why the model is called 2 - 1/2 dimensional. The particles which hit the walls are reflected according to the method desiqnated (I) in Ref.(24), which produces neither macroscopic plasma flows nor density perturbations near the walls.

The initial current profile used in the computer simulation is

$$j_z(x) = -n_0 e v_{dz} \exp - \{(\ell n 2)(x - L_x/2)^2/a^2\} \quad . \tag{40}$$

Here v_{dz} is the electron drift velocity in the z direction. The initial ion and electron temperature are taken to be uniform. The initial density profile balances the magnetic pressure produced self-consistently by the initial current:

$$n(x)(T_i + T_e) + B_y^2(x)/8\pi = \text{const.} \qquad (41)$$

The particle guiding centers are initially loaded according to the density profile. Physical parameters are $N_i=N_e=17424$, $L_x=64\Delta$, $L_y=64\Delta$, $\omega_{ce}/\omega_{pe}=1.5$, $c/v_{the}=10$, $\lambda_{De}=\Delta$, $m_i/m_e=16$, $T_i=T_e$, and $v_{dz}=-v_{the}$. Here N_i is the number of ions, N_e the number of electrons, and Δ the mesh size. Then the ion Larmor radius is 2.7Δ, and the electron Larmor radius is 0.67Δ. The ion cyclotron frequency ω_{ci} is $0.094\omega_{pe}$.

§4 Simulation results

In this section, results of several computer simulations are presented and compared with the theoretical predictions.

(A)

We first present the results of the simulation for the case $k_y a=0.5$, for which the mode with $k_y=\pi/32$ is unstable. The time evolution of the magnetic field lines projected on the x-y plane is shown in Fig.4, which displays double periodicities in the y direction. Clearly the formation and the growth of a magnetic island with $Re\omega=0$ are observed at the rational surface which lies on the line $x=L_x/2$. The magnetic island is formed at an early time, and its shape is not as symmetric along the y direction as along the x direction. Symmetry is established at $\omega_{pe}t=500$. Until this time the peaking of the current layer at the x-type neutral point leads mainly to the formation of a magnetic island; this corresponds to the linear phase. After $\omega_{pe}t=500$ the width of island becomes much larger.

In this phase ($\omega_{pe}t$=500 to 1000), the growth of the island is enhanced by the breaking of the current layer at the x-type neutral point, but not by the peaking of the current layer at that point. At $\omega_{pe}t$=1000 the mode has saturated, after which island remains stable. The saturation width is about $13\lambda_{De}$.

Fig.5 shows the time evolution of the current layer. At $\omega_{pe}t$=450, current peaking is observed at the x-type neutral point even though its amplitude is small. We also observe that the current layer already begins to break there. At $\omega_{pe}t$=650 the breaking has progressed further, and flatting of the current at the O-type neutral point is observed. We find that the current has diffused and that its width becomes larger than the initial one. The initial current has also changed from a layer to a lump as the instability grows. After saturation, the breaking of the current at the x-type neutral point becomes not as remarkable as that seen at $\omega_{pe}t$=1200, because the current-carrying electrons trapped in the magnetic island leak out through the $\underset{\sim}{E} \times \underset{\sim}{B}$ drift.

We can relate the induced electric field and the magnetic island in Fig.6. Fig.6b describes the magnetic field lines which are the same as Fig.4, whereas Fig.6a displays the contour lines of the induced electric field. At an x-type neutral point, the induced electric field has a positive peak, but has a negative peak at the O-type neutral point. These correspond to the particle acceleration mechanism of the tearing mode. It is observed that the induced electric field ranges over the entire plasma region and is not localized as it is during its growth.

The growth of the perturbed current-density, Fourier-analyzed in the y direction, is illustrated in Fig.7. This perturbed current density is localized in the x direction and its width is about that of the singular layer. We consider quantities averaged over some range in the x direction; i.e.,

$$j_{zm} = \frac{1}{2\Delta_x L_y} \int_{L_x/2-\Delta_x}^{L_x/2+\Delta_x} dx \int_0^{L_y} dy\, j_z \exp -ik_y y \quad , \qquad (42)$$

$$k_y = 2\pi m/L_y \quad .$$

We choose $\Delta_x = 5\Delta$ in Fig.7a. The solid line in this figure has the slope obtained from the linear theory in Sec.2 (see Eq.10). During early times ($\omega_{pe}t=0$ to 250), all modes relax to the thermal level, which is $|j_{zm}|/j_{oz} \sim 4 \times 10^{-2}$, $m \geq 1$. The m=1 mode is unstable in this case, and after $\omega_{pe}t=250$ the mode grows above the thermal level, whereas the high-m modes continue to fluctuate around the thermal level, as predicted by the linear theory. During $\omega_{pe}t=250$ to 500, the m=1 mode grows up with the growth rate of linear theory. In the nonlinear phase (after $\omega_{pe}t=500$), the growth rate becomes slightly larger. This nonlinear phase occurs when the initial current changes its profile and becomes diffuse [see Fig.5]. After the magnetic island has grown to some degree, the electrons in the singular layer are trapped and begin bounce motions in the island. The electrons' bounce frequency ω_b is given by,[15]

$$\omega_b = k_y v_{the} w/2\ell_s \quad . \qquad (43)$$

where w is the width of the magnetic island. If this bounce

frequency becomes larger than the growth rate, the electrons experience an average induced electric field along the closed field lines and are no longer accelerated by the electric field. In the nonlinear phase ($\omega_{pe}t$=500 to 1000), of Fig.7a, ω_b is measured to be from 2×10^{-3} ω_{pe} to 3.8×10^{-3} ω_{pe} in value; the linear growth rate is 1.72×10^{-3} ω_{pe}. Therefore, in this phase, acceleration of electrons does not occur, so the mechanism of the instability differs from that of the tearing mode. The induced electric field produces a charge separation along and also across the magnetic field lines. The resultant $\underset{\sim}{E} \times \underset{\sim}{B}$ drifts mostly distort the initial current, which enhances the growth rate of the instability.

This situation is displayed more clearly in Fig.7b. The open circles correspond to Δ_x= 10Δ and solid circles to Δ_x=5Δ in this figure, which shows the time evolution of the instability in Fig.7a. The m=1 mode, shown by open circles, behaves in time the same as that mode corresponding to the solid circle, before $\omega_{pe}t$=500. However, in the nonlinear phase, the growth rate of the m=1 mode is greatly enhanced compared with the solid circles mode. This indicates that the current layer distorts at both edges of magnetic island. Moreover, the total current (i.e. the m=0 mode)decays greatly in this phase. At $\omega_{pe}t$=1000, the m=1 mode saturates to a value $|j_{z1}|/j_{oz} \sim 2 \times 10^{-1}$. After $\omega_{pe}t$=1000 the amplitude of m=1 mode changes little. Mode-mode coupling is not observed at anytime.

Fig.8 shows the time evolution of the electrostatic field across the singular layer. The electrostatic field is Fourier-analyzed in the y direction. The m=2 and m=3 modes do not

grow but rather fluctuate throughout the simulation run. The m=1 mode, however, grows from $\omega_{pe}t=250$ to 500 at the growth rate, $\gamma \simeq 4.0 \times 10^{-3}\omega_{pe}$, which is larger than the linear growth rate. This growth rate agrees with that of the vector potential, to be discussed later. At $\omega_{pe}t=550$, the m=1 mode saturates. The amplitude of the mode begins to decrease at $\omega_{pe}t=800$ and has damped out at $\omega_{pe}t=1000$. This forms a striking contrast to the behavior of the m=1 mode for the perturbed current; specifically, the growth rate of the perturbed current increases at $\omega_{pe}t=500$. (B)

To confirm that electrostatic effects increase the growth rate of the instability and distort the initial current anomalously, we next present the results of the simulation excluding electrostatic effects. This simulation is carried out in such a way that the term $E_L(\underset{\sim}{r})$ in the equation of motion (Eq.39) may be neglected without loss of self-consistency. The physical parameters used here are the same as those for the simulation including electrostatic effects.

Fig.9 shows the time evolution of the perturbed current density, Fourier analyzed in the y-direction. $\Delta_x=5\Delta$ is chosen in Fig.9a. The slope of the solid line in this figure corresponds the linear growth rate. All modes relax to the thermal level $|j_{zm}|/j_{oz} \sim 4 \times 10^{-2}$, until $\omega_{pe}t=500$. High-m modes fluctuate around the thermal level throughout the simulation run. The m=1 mode growth rate agree with the linear growth rate during the period $\omega_{pe}t=500$ to 1000. At $\omega_{pe}t=1000$, the amplitude saturates. However the mode begins to grow again at $\omega_{pe}t=1300$ with a smaller growth rate ($\sim 8.0 \times 10^{-4}\ \omega_{pe}$) compared with that of linear phase.

This mode saturates finally at $\omega_{pe}t=2400$, and thereafter the amplitude does not change.

There appear some features of the growth different from that which includes electrostatic effects. In the linear phase, the source of instability is the acceleration of electrons by the induced electric field, and the magnetic island is formed by the peaking of the current layer, even though the amplitude of the peaking is too small to be observed at the x-type neutral point. However the electrons in the singular layer become trapped in the magnetic island and are not accelerated when the electron bounce frequency ω_b is nearly equal to the growth rate of the instability. At $\omega_{pe}t=1000$, the instability saturates temporarily, at which time ω_b is measured to be about $1.7 \times 10^{-3}\omega_{pe}$. This ω_b agrees well with the linear growth rate.

After $\omega_{pe}t=1000$, the electrons are no longer accelerated by the induced electric field. During the growth of the amplitude from $\omega_{pe}t=1300$ to 2400, the initial current profile changes greatly, corresponding to the phase in Fig.7a between $\omega_{pe}t=500$ and 1000. We plot the time evolution of the instability for $\Delta_x=10\Delta$ with open circles in Fig.9b. The solid circles refer to the case of $\Delta_x=5\Delta$. Notice that, while the solid circles grow nearly with the linear growth rate, the open circles grow with a lower growth rate during $\omega_{pe}t=500$ to 1000 because the instability is localized in the narrow singular layer. However when the solid circles saturate temporarily, the open circles continue to grow indicating that the current layer has been distorted by the effects, for example, of $\tilde{E}_{zt}\hat{e}_z \times B$ drifts, except for the electrons' acceleration by $\tilde{E}_{zT}\hat{e}_z$, because the $\tilde{E}_{zT}$ ranges over

the whole plasma even for the simulation excluding electrostatic effects. The open circles grow at an enhanced growth rate from $\omega_{pe}t=1500$ on and then saturate at $\omega_{pe}t=2000$. The value of the saturated amplitude is the same as for the case $\Delta_x=5\Delta$. The total current (m=0 mode) in the layer ($\lesssim 5\Delta$) diffuses greatly during the time that the growth rate of the m=1 mode is enhanced, i.e., from $\omega_{pe}t=1500$ to 2300. Mode-mode coupling is not observed in this simulation.

So far we have mainly discussed the time evolution of the perturbed current density, because it has some conspicuous features between the linear and nonlinear phases. However this current perturbation is localized in the singular layer, so its growth rate depends sensitively on Δ_x in Eq.(42). Fig.10 shows the time evolution of the perturbed vector potential, which is assumed to be constant in the singular layer and not so sensitive to the choice of Δ_x. The results shown in Fig.10a include the electrostatic effects, whereas those of Fig.10b exclude them. The vector potential is Fourier-analyzed in the y direction and averaged over some range in the x direction according to Eq.(42). We choose $\Delta_x=6\Delta$ in both figures. In Fig.10a, the m=1 mode is seen to be unstable and growing with the grwoth rate ($\sim 4.0 \times 10^{-3}\omega_{pe}$) from $\omega_{pe}t=250$ to 500, which is greater than that derived from the linear theory excluding electrostatic effects. In the nonlinear phase after $\omega_{pe}t=500$, the growth rate becomes slightly larger compared with that in the linear phase. At $\omega_{pe}t=1000$, the mode has saturated. In Fig.10b the growth rate of the m=1 mode is smaller than that in Fig.10a at first sight. A solid line in Fig.10b corresponds

to the linear growth rate of Eq.10. The m=1 mode grows nearly with the linear growth rate between $\omega_{pe}t$=500 to 800. At $\omega_{pe}t$=800 this mode begins to saturate temporarily. However the mode begins to grow again with a lower growth rate ($\sim 1.3 \times 10^{-3}\omega_{pe}$) after $\omega_{pe}t$=1000, and then saturates at $\omega_{pe}t$=2400. The saturation level is the same in both cases.

Let us now examine the transport due to the tearing mode instability. It is particularly interesting to know the diffusion of the initial current layer. (We have already shown the decay of the averaged initial current in Fig.7b and in Fig.9b.) We illustrate the time evolution of the total current in Fig.11. The total current is little changed from the initial profile at $\omega_{pe}t$=400 because the amplitude of the unstable mode is small. However the profile relaxes as the mode grows nonlinearly. At $\omega_{pe}t$=800 both of its edges have been cut down. After saturation, its profile has been flattened. In the case of excluding electrostatic effects, relaxation also occurs but that the relaxation time is long and cutting down at the edges is not observed.

We now investigate the current relaxation more quantitatively. We have already derived the current diffusion equation (Eq.18) in the linear phase in section 2.2. We now compare the theory and the observed diffusion rate in the nonlinear phase. In the nonlinear phase electrons are not accelerated. Then, Eq.(18) is reduced to

$$\frac{\partial}{\partial t} j_z = \frac{\partial}{\partial x} D_j \frac{\partial}{\partial x} j_z \quad . \tag{44}$$

Where D_j is given in Eq.(20). From Eq.(44), the relaxation of the current averaged over x becomes:

$$\frac{\partial}{\partial\omega_{pe}t}\log|\bar{j}_z| = \left(\frac{\tilde{B}_{kx}}{B_z}\right)^2\frac{\gamma_k}{\bar{v}_{oz}^2}\,A \quad . \tag{45}$$

where

$$\bar{j}_z = \frac{1}{2\ell_x L_y}\int_{L_x/2-\ell_x}^{L_x/2+\ell_x} dx\int_0^{L_y} dy\; j_z, \quad \bar{v}_{oz} = \frac{1}{2\ell_x}\int_{L_x/2-\ell_x}^{L_x/2+\ell_x} dx\; v_{oz},$$

$$A = \frac{4(\ell n2)(l\omega\omega)\omega_{ce}^2c^4}{\omega_{pe}^4k_y^2\ell_x a^2}\exp-[(\ell n2)\ell_x^2/a^2]\Big/\int_{-\ell_x}^{\ell_x} dx\,\exp-[(\ell n2)x^2/a^2].$$

The solid line in Fig.12 corresponds to Eq.(45). Here $\ell_x=5\Delta$ is chosen. The points in Fig.12 are the diffusion rate measured from several simulation runs. In the simulation, the quantity $\partial\log|\bar{j}_z|/\partial\omega_{pe}t$ can be measured, for example, from the decay rate of the m=0 mode in Fig.7a. The growth rate of the vector potential is used for γ_k in Eq.(45). $\tilde{B}_{kx}$ is known from the amplitude of the vector potential. Then the right side of Eq.(45) is determined in the simulation. We performed simulation runs for several values of the half width "a" of the current layer. The open circles in Fig.12 are for when electrostatic effects are excluded, and the others are with them. Particularly, in the nonlinear phase, the growth rate γ_k, and also the amplitude of $\tilde{B}_{kx}$, varies with time. Then, we can obtain many points from the same simulation. This is the reason why there are several points having the same shape in Fig.12. The agreement between the theory and the simulation results is very good.

Fig.13 describes the time evolution of the width of the magnetic island for $k_y a=0.5$. Fig.13a is with electrostatic effects, and Fig.13b is without. In the linear and nonlinear phase, the growth of the width of magnetic island is almost proportional to time. Its saturated width is nearly the same for both cases.

We now consider the saturation mechanism of tearing modes. Noting that the saturation level is the same for simulations both with and without electrostatic effects, we conclude that the electrostatic effects may not contribute to saturation. Next, we consider whether the ion tearing mode[13] takes part in the nonlinear growth phase. If it occurs, then the saturation of the ion acceleration by the induced electric field is expected as for electrons. However, this effect does not act as the saturation mechanism because the growth rate in the nonlinear phase is different in both simulations. However, the current diffusion due to quasilinear effects may play an important role in saturation. The current profile averaged over the y direction at the saturated time of instability is illustrated in Fig.14 for several simulations. Their profiles resemble each other and the half width is roughly the same, $k_y a \simeq 1.0$. Thus, a saturation mechanism may be that the initial current diffuses quasilinearly to become stable for the tearing mode; i.e., it enters the region $\Delta' < 0$, even though the mechanism for the instability in the nonlinear phase is still unknown.

(C)

So far we have focused on single-mode tearing; i.e., only one mode is unstable in the system. We now investigate multi-

mode tearing in particular, the system in which two modes are unstable. The results of the simulation (including electrostatic effects) for the case $k_y a = 0.2$ and $v_{dz} = -2\, v_{the}$ are presented. Other physical parameters are the same as for the single-mode tearing problem. Here, the modes $k_y = \pi/32$ and $\pi/16$ are unstable. Fig.15 shows the time evolution of the magnetic field lines projected on the x-y plane. Double periodicities in the y direction are visible. At $\omega_{pe}t=150$, double magnetic islands have already been formed. These magnetic islands are not symmetric, because two modes are growing. The growth saturates temporarily at $\omega_{pe}t=300$. However, the two islands begin to combine at $\omega_{pe}t=600$ after the stable state goes on for some time. At $\omega_{pe}t=850$ their combination produces one large magnetic island. The magnetic island in this phase is stable until the end of the simulation run.

Fig.16 is a three-dimensional display of the current profile at various times. At $\omega_{pe}t=150$, the current layer begins to break up. At $\omega_{pe}t=300$, two current cylinders of different magnitude are formed. These cylinders exist stably for a while. However, the two cylinders begin to be drawn toward each other at $\omega_{pe}t=500$ and fuse at $\omega_{pe}t=800$. With the fusion, the expansion of the lump of current takes place in the x direction. At $\omega_{pe}t=850$, a double-humped current profile appears. This expansion continues until $\omega_{pe}t=1000$. At $\omega_{pe}t=1100$ one large current cylinder of radius about 10Δ is formed. Fig.17 describes the time evolution of the perturbed vector potential. The vector potential is treated according to Eq.(42) and Δ_x is chosen to be 3Δ. First, until $100\omega_{pe}^{-1}$, all modes relax to their

thermal level. During $\omega_{pe}t$=100 to 200, the m=1 and m=2 modes grow with nearly the same growth rate $\gamma \sim 1.2 \times 10^{-2}\omega_{pe}$. The m=1 mode saturates at $\omega_{pe}t$=200 temporarily, which quasi-steady state continues until $\omega_{pe}t$=500. However, at $\omega_{pe}t$=550 the m=1 mode begins to grow again and finally saturates at $\omega_{pe}t$=800. However, m=2 mode grows until $\omega_{pe}t$=300 and then saturates. After this time the amplitude of the m=2 mode decreases slowly and then suddenly dumps at $\omega_{pe}t$=650. However, at $\omega_{pe}t$=800 the m=2 mode begins to grow and dumps again at $\omega_{pe}t$=1000.

In this simulation of multi-mode tearing, the electron acceleration along the magnetic field lines excites this instability only in the early times, i.e., before $\omega_{pe}t$=200. Even in this pahse, however, the peaking of the current layer is not observed. Instead, the current layer breaks up. Therefore, the main effect producing the two current cylinders may be the $\underset{\sim}{E} \times \underset{\sim}{B}$ drifts. After $\omega_{pe}t$=200, the system is stable to tearing modes because the x-type neutral point is outside of the current cylinders. However, the system is never stable, since the two current cylinders are attracted to each other as long as the currents flow in the same direction. Then finally one current cylinder is produced by the combination of the two. The mechanism for which differs from that for the tearing modes.

§5 Conclusions and Discussions

We have described the behavior of single-mode and multi-mode tearing and the anomalous transport associated this instability both analytically and with computer simulations. We found that tearing modes grow through three phases: the phase when the mode grows with the linear growth rate by means of the acceleration of electrons; the one when the acceleration ceases and the growth saturates temporarily; the third phase when the mode grows nonlinearly. During this third phase, the current is pinched by $\tilde{E}_z\hat{e}_z \times \underset{\sim}{B}$ drifts (or $\tilde{j}_z\hat{e}_z \times \underset{\sim}{B}$ forces in terms of fluid terminology). In this last phase the electron inertia only prevents the divergence of current at the x-type neutral point as was pointed out by Dungey.[25]

We have confirmed that electrostatic effects enhance the linear and nonlinear growth rate of the tearing mode. Our simulation results show that their effects on the growth rate tends to increase the magnetic island grows.

We also showed that the current diffusion coefficient, given by Eq.(20), is due to the effect of current-carrying electrons diffusing along perturbed magnetic field lines. It should be noted that the diffusion observed in the simulation agreed well with Eq.(20) and Eq.(44) at each time, not averaged in time. The width of the magnetic island is observed to grow proportionally to time in the nonlinear phase. The saturation mechanism was investigated, and we suggested that the initial current layer diffused quasi-linearly to become a stable region, ($\Delta' < 0$). However, it is not clear that the linear

stability criterion, $\Delta' < 0$, is applicable to the nonlinear phase because the mechanism of instability is different. Two magnetic islands were observed to combine with each other in the simulation of multi-mode tearing. This indicates that low amplitude, high-m number tearing mode finally forms large amplitude, low-m number magnetic islands. Therefore these phenomena can be expected to greatly enhance the anomalous plasma transport.

Acknowledgements

The authors would like to acknowledge the useful discussions and encouragement of Dr. M. Wakatani. They are grateful to Drs. H. Sanuki, T. Hatori, Y. Terashima and Y. Ohsawa for their valuable discussions and criticism. They also wish to thank Mr. J. Van Dam for his critical reading of this manuscript and to the members of the computer center of the Institute of Plasma Physics, Nagoya University, for their assistance with the computer simulations.

References

1) O. Kluber, F. Kangen and G. Fussmann, BAPS 21, 1050(1976)

2) R.D. Hazeltine and H.R. Strauss, Phys. Rev. Lett. 37, 102 (1976)

3) H.P. Furth, J. Killeen and M.N. Rosenbluth, Phys. Fluids 6, 459 (1963)

4) H.R. Hicks, B. Carreras, J.A. Holmes and B.V. Waddel, ORNL/TM-6096, (December 1977)

5) D. Biskamp, IPP6/163 (August 1977)

6) D.D. Schnack, UCRL-52399 (January 1978)

7) B.V. Waddel, M.N. Rosenbluth, D.A. Monticello and R.B. White, Nucl. Fusion 16, 528(1976)

8) A. Syke and J.A. Wesson, Phys. Rev. Lett. 37, 140(1976)

9) H.P. Furth, Nucl Fusion Suppl. Pt. 1, 169 (1962)

10) B. Coppi, Phys. Fluids 8, 2273(1965)

11) R.D. Hazeltine, D. Dobrott and T.S. Wang, Phys. Fluids 18, 1778(1976)

12) J.F. Drake and Y.C. Lee, Phys. Fluids 20, 1341(1977)

13) F.V. Coroniti, Phys. Rev. Lett. 38, 1355(1977)

14) A.A. Galeev and L.M. Zeleneyi, JETP Lett. 25, 380(1977)

15) J.F. Drake and Y.C. Lee, Phys. Rev. Lett. 39, 453(1977)

16) P.H. Rutherford, Phys. Fluids 16, 1903(1973)

17) A.A. Galeev, Phys. Fluids 21, 1353(1978) and see also E.G. Harris, Nuovo Cimento 23, 115(1962)

18) B.D. Fried and S.D. Conte, The Plasma Dispersion Function, (Academic Press, N.Y., 1961)

19) J. Wesson, Nucl. Fusion 16, 130(1966)

20) C.W. Nielson and H.R. Lewis, Methods in Computational Physics 16, (Academic Press, 1976) p367

21) J. Busnardo-Neto, P.L. Pritchett, A.T. Lin and J.M. Dawson, J. Comp. Phys. 23, 300(1977)

22) see, for example, A.B. Langdon and C.K. Birdsall, Phys. Fluids 13, 2115(1970)

23) W.L. Kruer, J.M. Dawson and B. Rosen, J. Comp. Phys. 13, 114(1973)

24) H. Naitou, S. Tokuda and T. Kamimura, Internal Report of Institute of Plasma Physics, Nagoya University, IPPJ-307 (1977)

25) J.W. Dungey, Cosmic Electrodynamics (Cambridge University Press, New York, 1958), pp.98-102.

Figure Captions

Fig.1 Equilibrium current distribution shown in slab geometry bounded by conducting walls in the x direction. The current flows in the z direction producing a sheared field $B_s << B_0$.

Fig.2 Linear growth rate obtained from Eq.(10) for the case $j_{oz}=en_0(T_e/m_e)^{1/2}$. The eigenfunction of vector potential A_z is shown in (b).

Fig.3 Topology of the x-type neutral point projected on the x-y plane. The long arrows show the direction of the electron motion accelerated by the induced electric field. The short arrows show the direction of electron flow which is produced by the electrostatic fields.

Fig.4 Magnetic field lines projected on the x-y plane with double periodicity in the y direction.

Fig.5 Three-dimensional displays of the current layer with double periodicity in the y direction.

Fig.6 Contour lines of the induced electric field, showing the mechanism of the instability. (b) is the magnetic field lines projected on the x-y plane.

Fig.7 Time evolution of the perturbed current density. $\Delta_x=5\Delta$ in (a) and also for the solid points in (b). The open points in (b) are for $\Delta_x=10\Delta$.

Fig.8 Time evolution of the electrostatic fields across the singular layer, Fourier-analyzed in the y direction.

Fig.9 Time evolution of the perturbed current density without electrostatic effects. (a) is the case $\Delta_x=5\Delta$ and solid

points are also $\Delta_x=5\Delta$. Open points in (b) are the case $\Delta_x=10\Delta$. The solid line corresponds to the linear growth rate.

Fig.10 Time evolution of the perturbed vector potential A_z. $\Delta_x=6\Delta$ is chosen in both figures. (a) is with and (b) is without electrostaric effects. The solid line in (b) corresponds to the linear growth rate.

Fig.11 Time evolution of the current profile (no electrostatic effects).

Fig.12 Current diffusion obtained from several simulations. Open circles are without electrostatic effects, and others are the case with them. Solid line corresponds to the theoretical diffusion rate.

Fig.13 Time evolution of the width of the magnetic island for $k_y a=0.5$. (a) is with electrostatic effects and (b) without.

Fig.14 Current profile when the instability has saturated. The slender solid line is with electrostatic effects, and others are for without.

Fig.15 Magnetic field lines projected on the x-y plane.

Fig.16 Three-dimensional displays of the current layer.

Fig.17 Time evolution of perturbed vector potential A_z. $\Delta_x=3\Delta$.

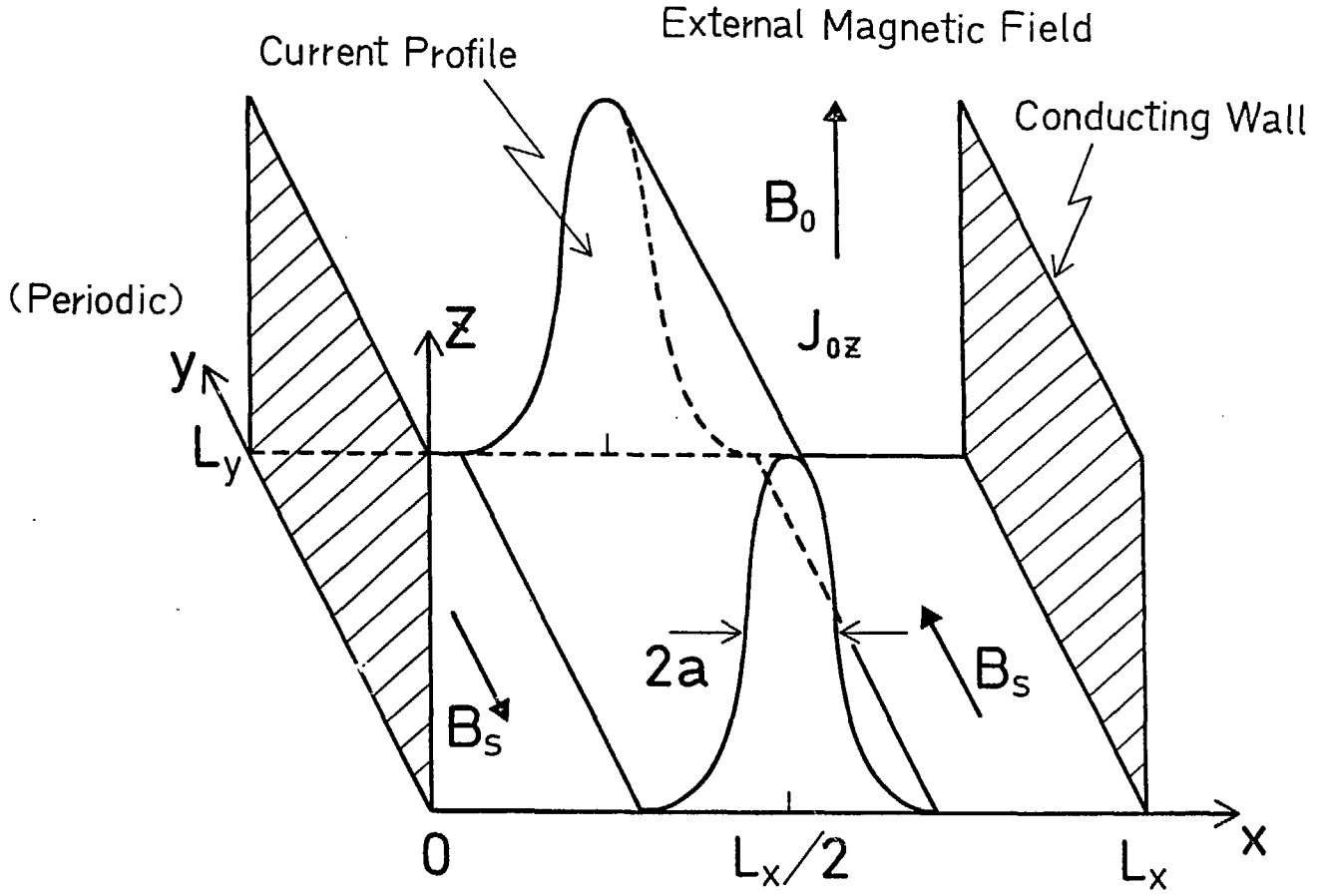
External Magnetic Field
Current Profile
Conducting Wall
B_0
(Periodic)
z
J_{0z}
y
L_y
2a
B_s
B_s
0
$L_x/2$
L_x
x

Fig.1

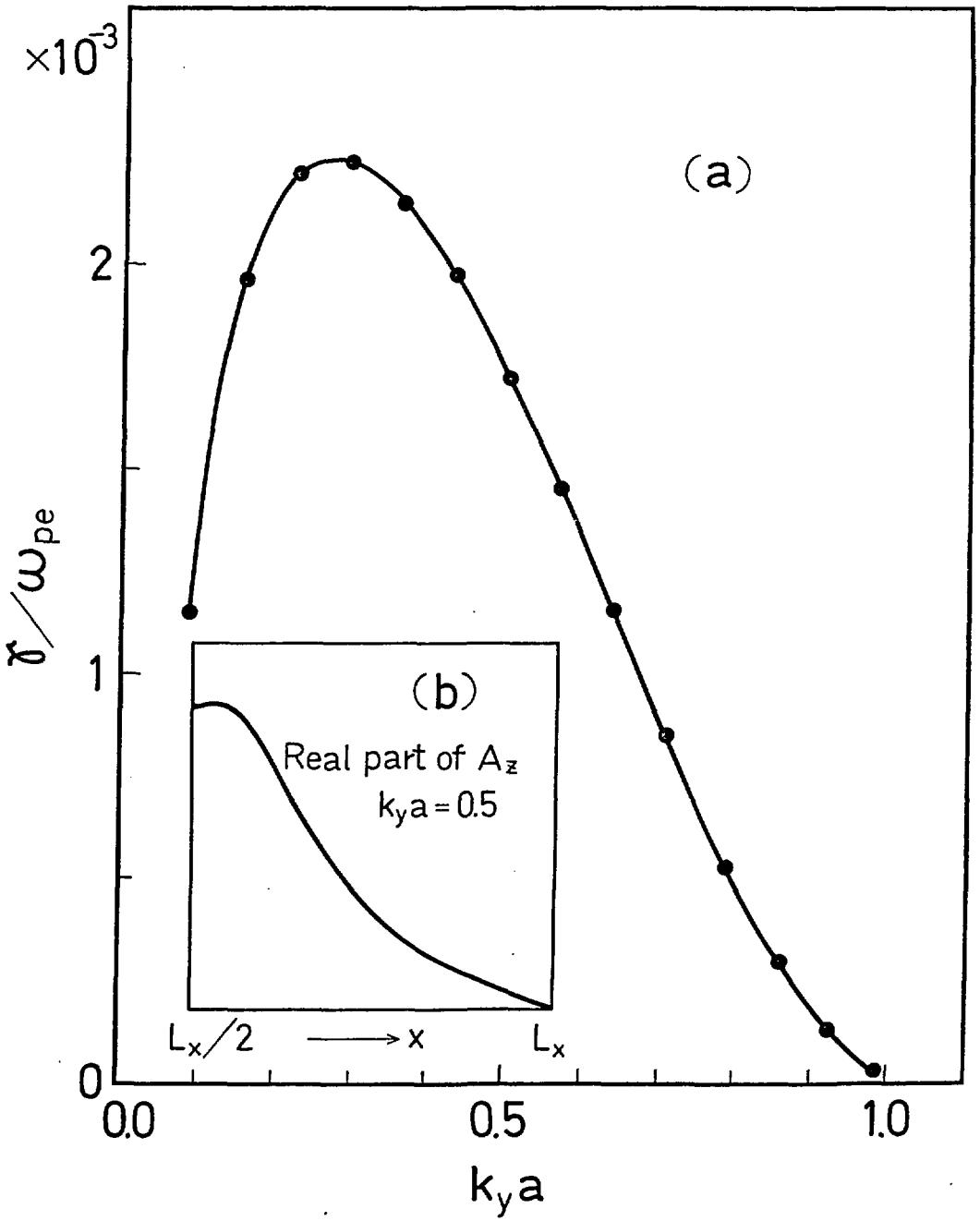

Fig.2

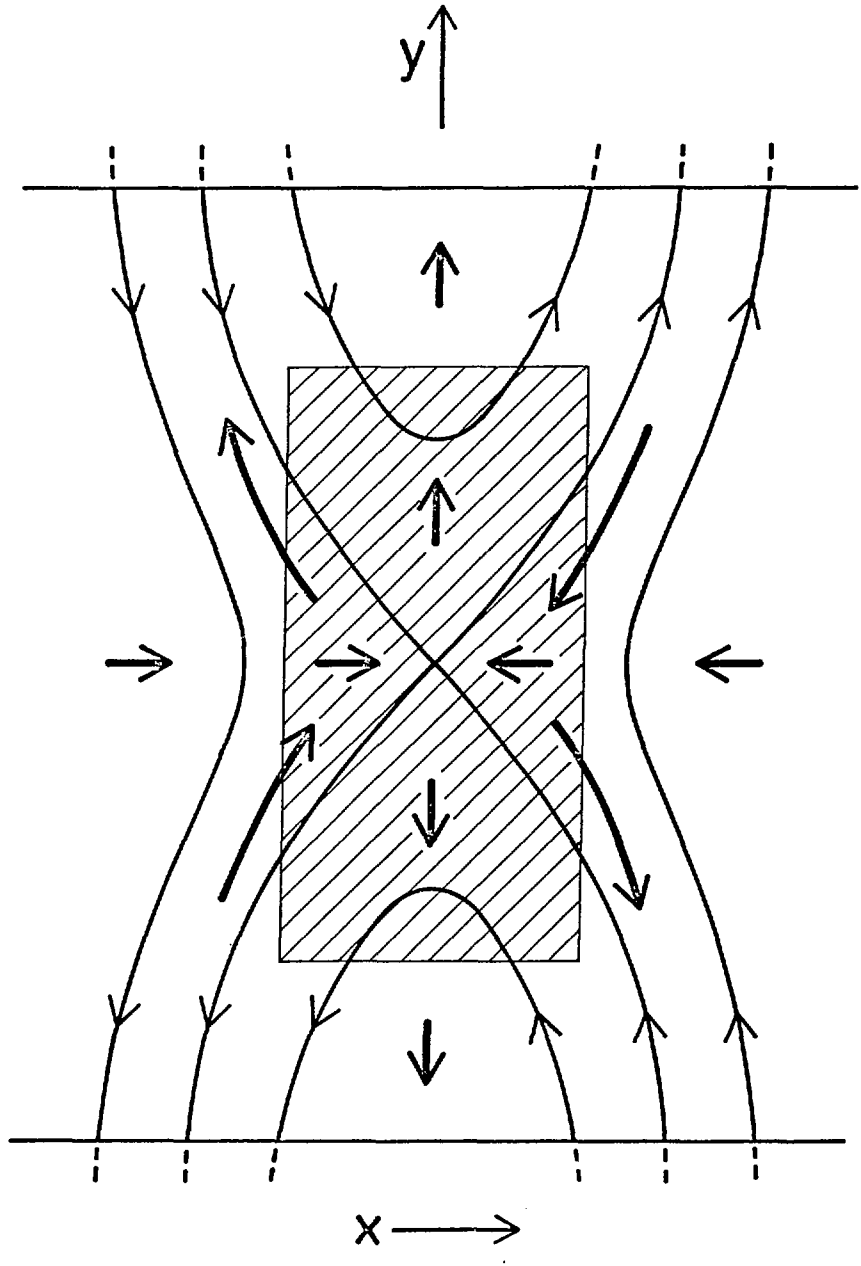

Fig.3

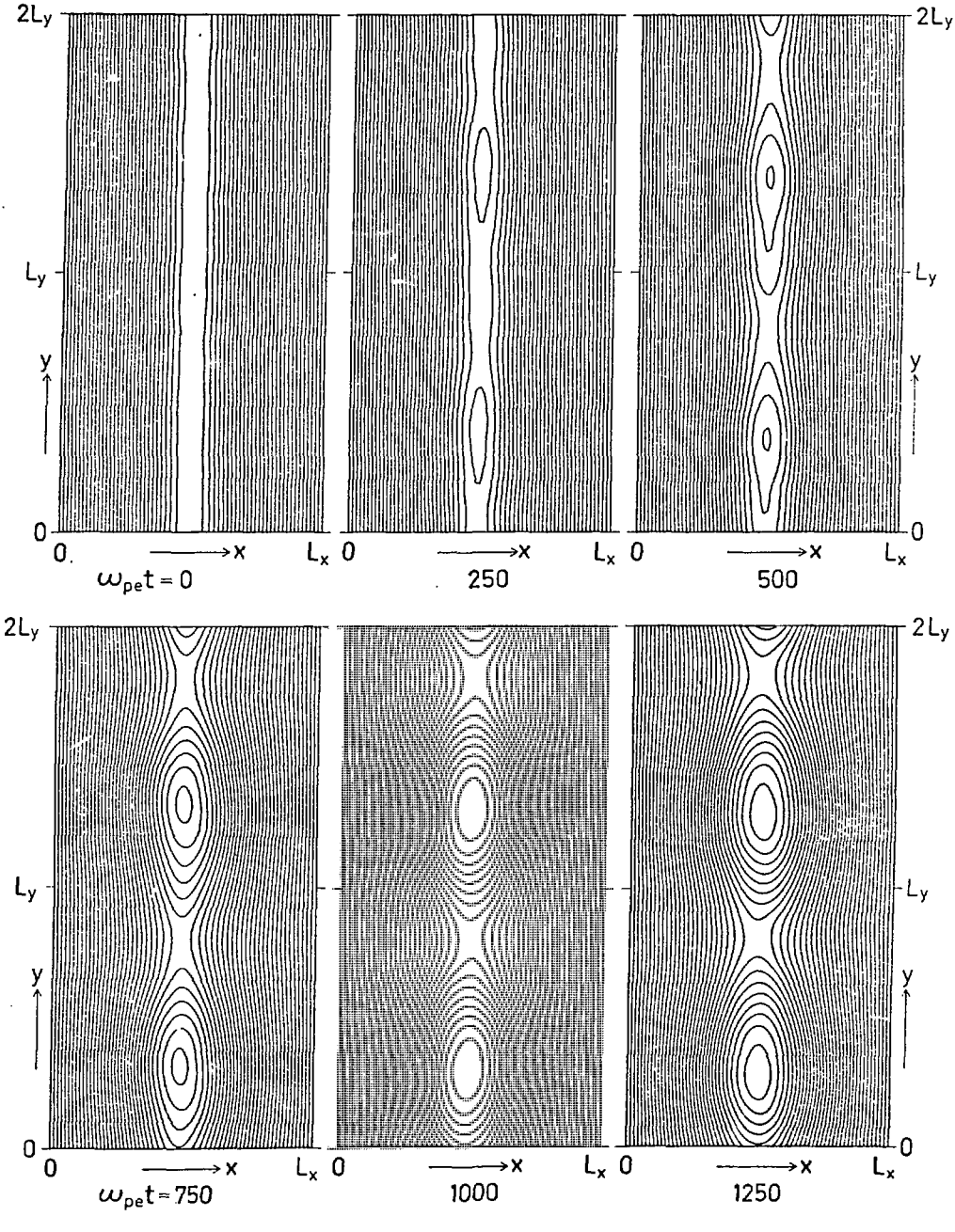

Fig.4

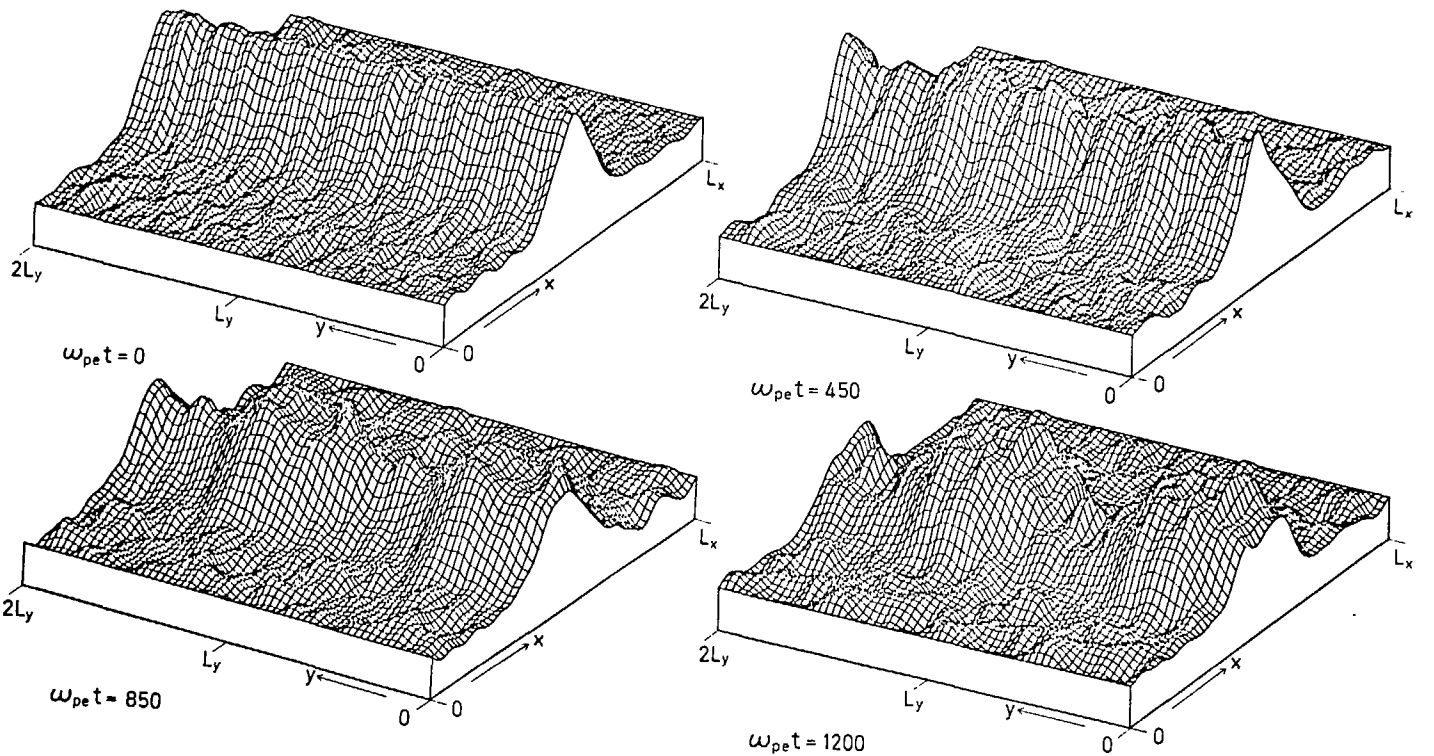
$\omega_{pe}t = 0$
$\omega_{pe}t = 450$
$\omega_{pe}t = 850$
$\omega_{pe}t = 1200$
$2L_y$
L_y
L_x
y
x
0

Fig.5

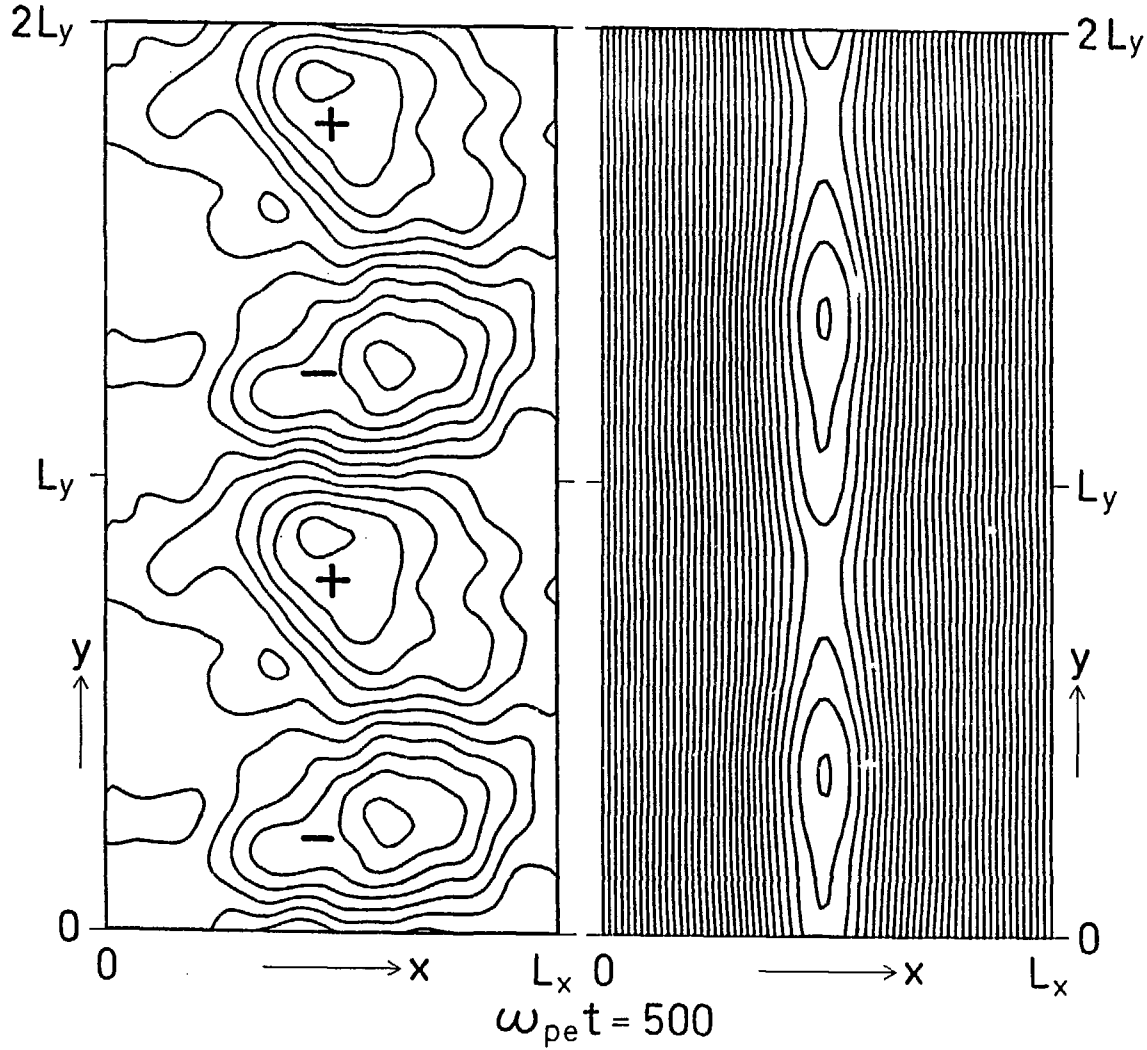

Fig.6

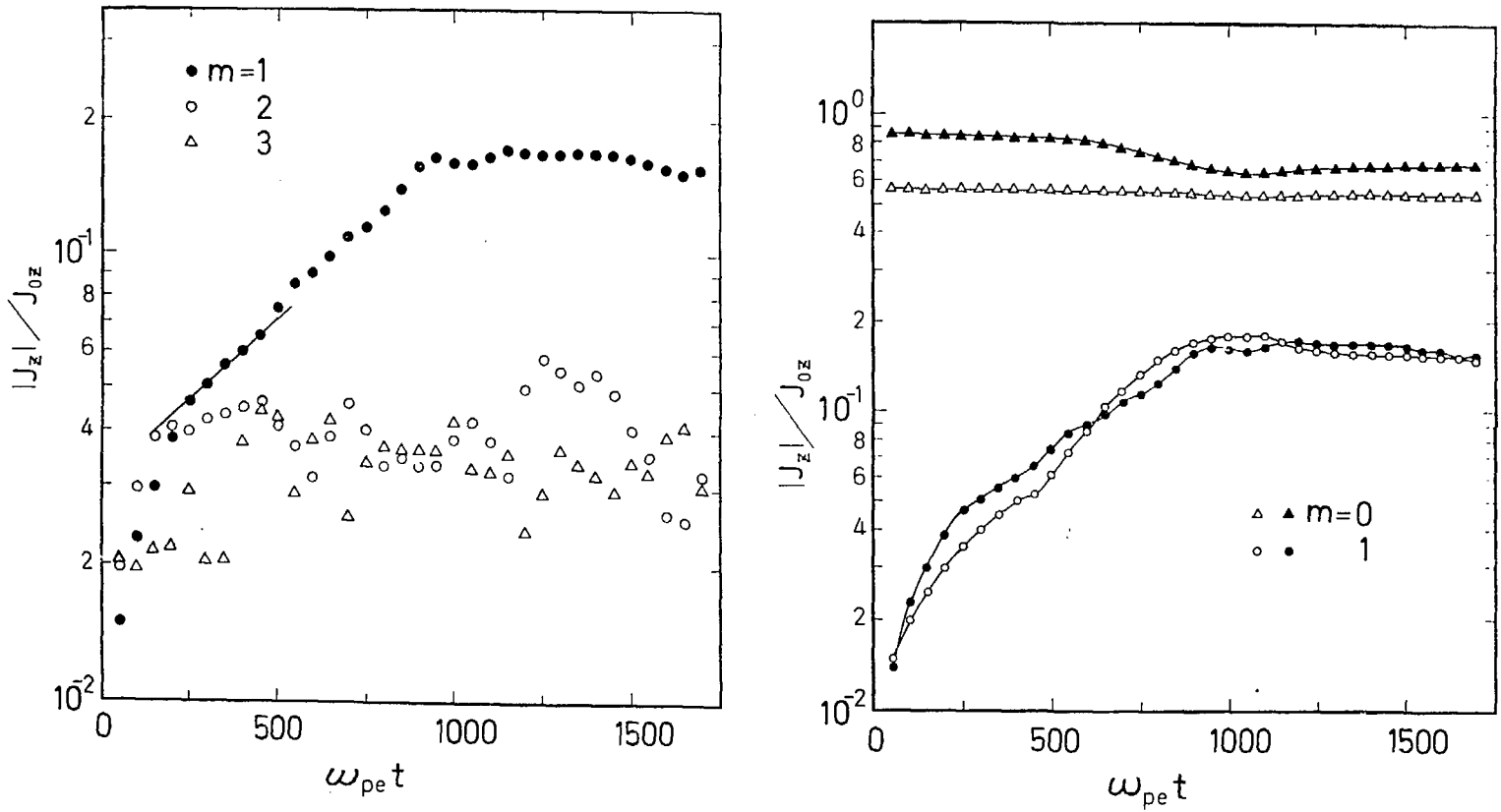

Fig.7

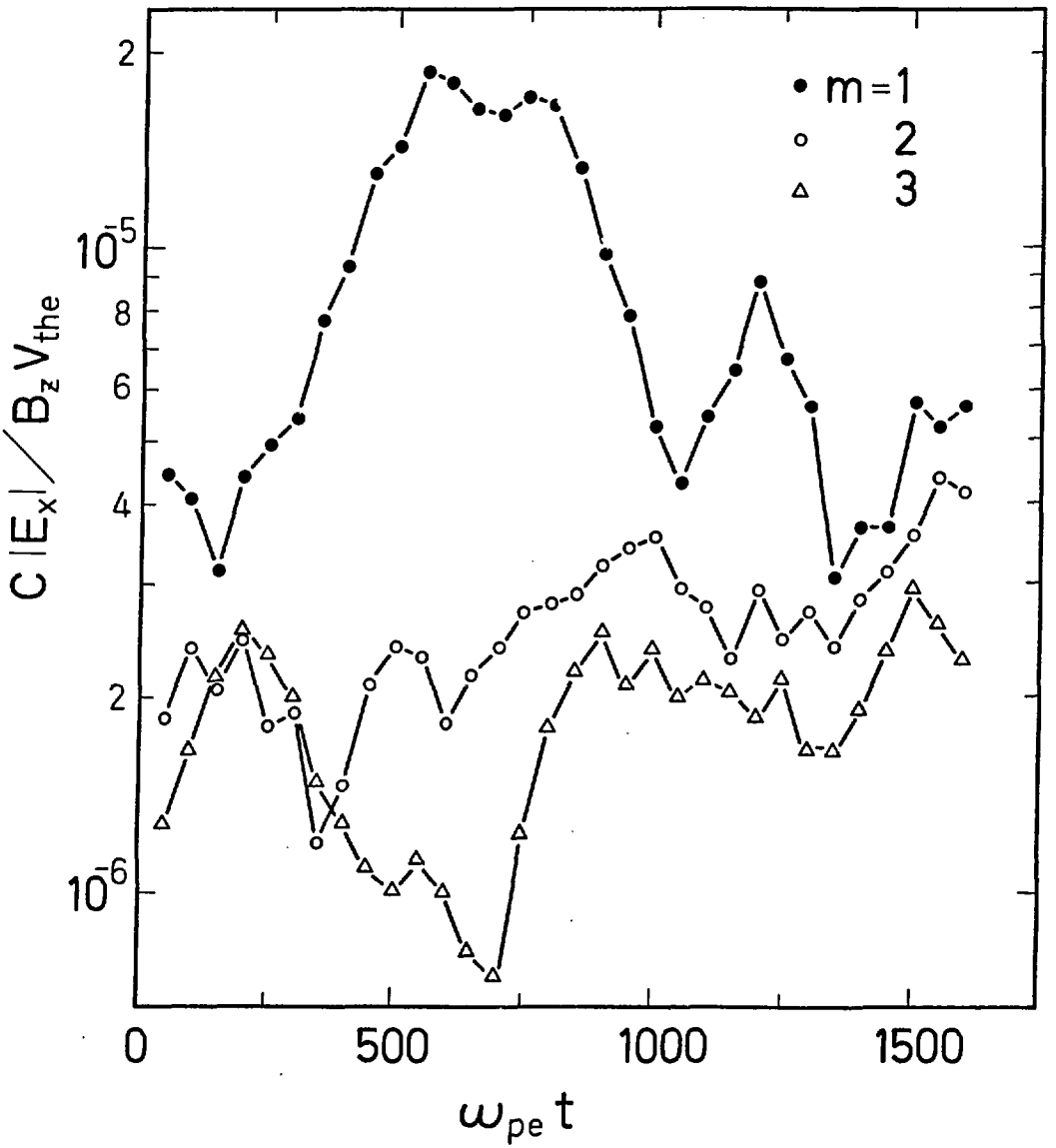

Fig.8

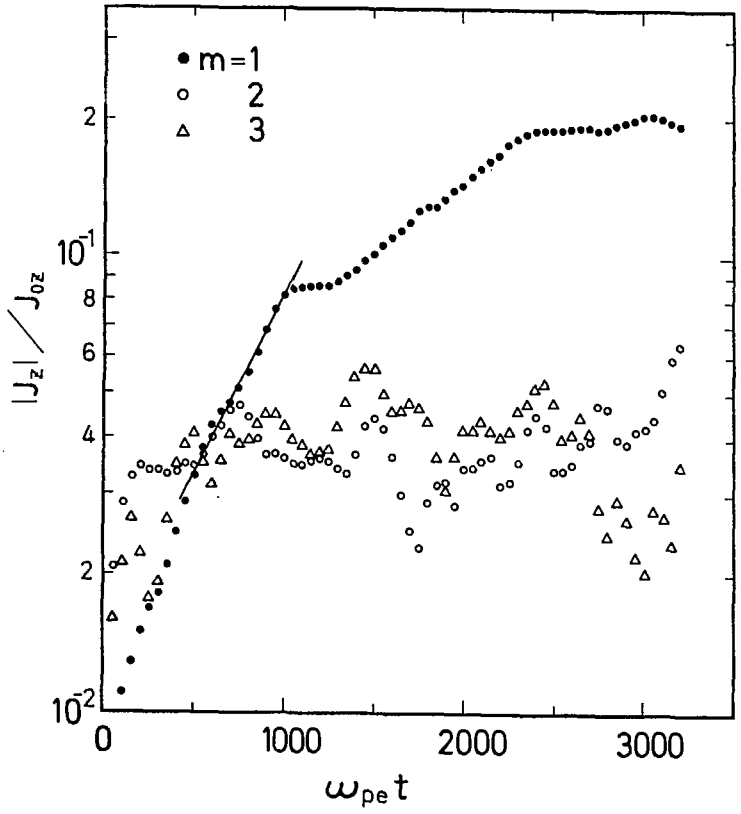
m=1
2
3
$|J_z| / J_{0z}$
10^{-1}
10^{-2}
0
1000
2000
3000
$\omega_{pe}\,t$

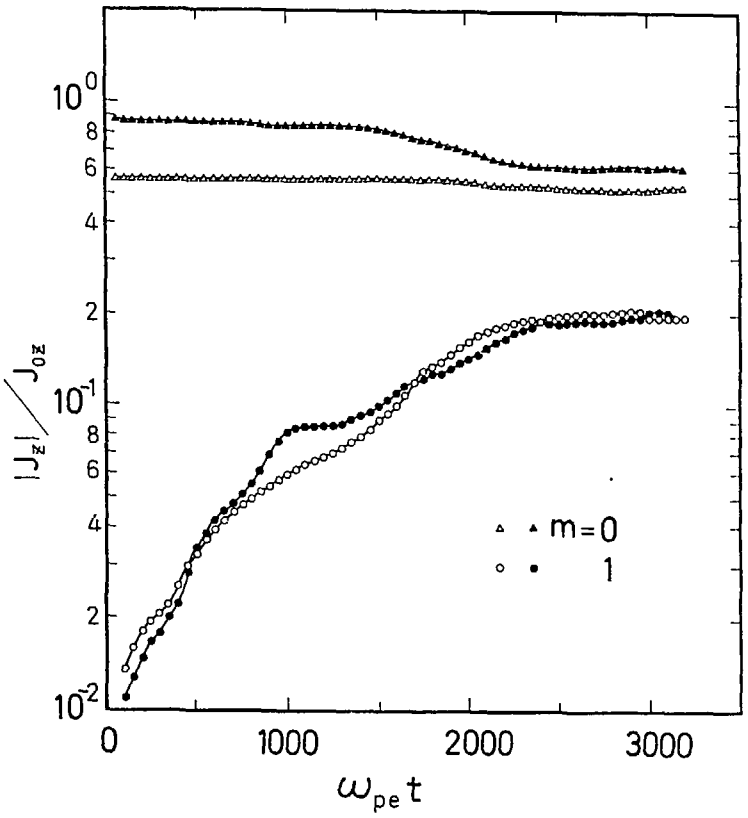
10^{0}
10^{-1}
10^{-2}
$|J_z| / J_{0z}$
m=0
1
0
1000
2000
3000
$\omega_{pe}\,t$

Fig.9

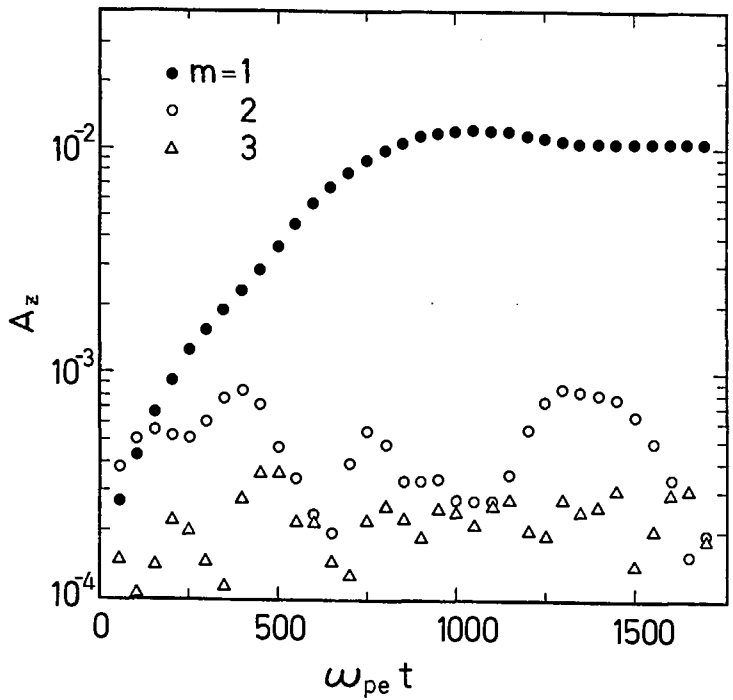
m=1
2
3
10^{-2}
10^{-3}
10^{-4}
A_z
0
500
1000
1500
$\omega_{pe}t$

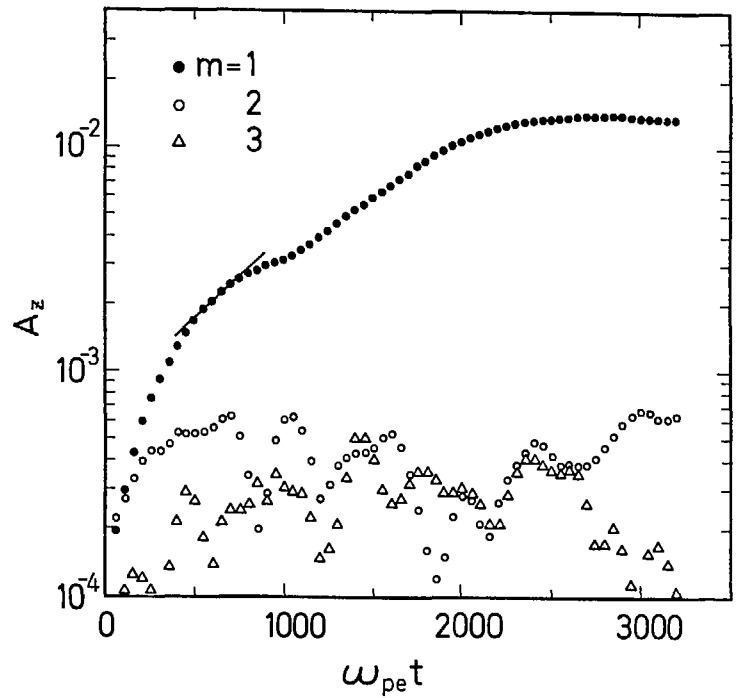
m=1
2
3
10^{-2}
10^{-3}
10^{-4}
A_z
0
1000
2000
3000
$\omega_{pe}t$

Fig.10

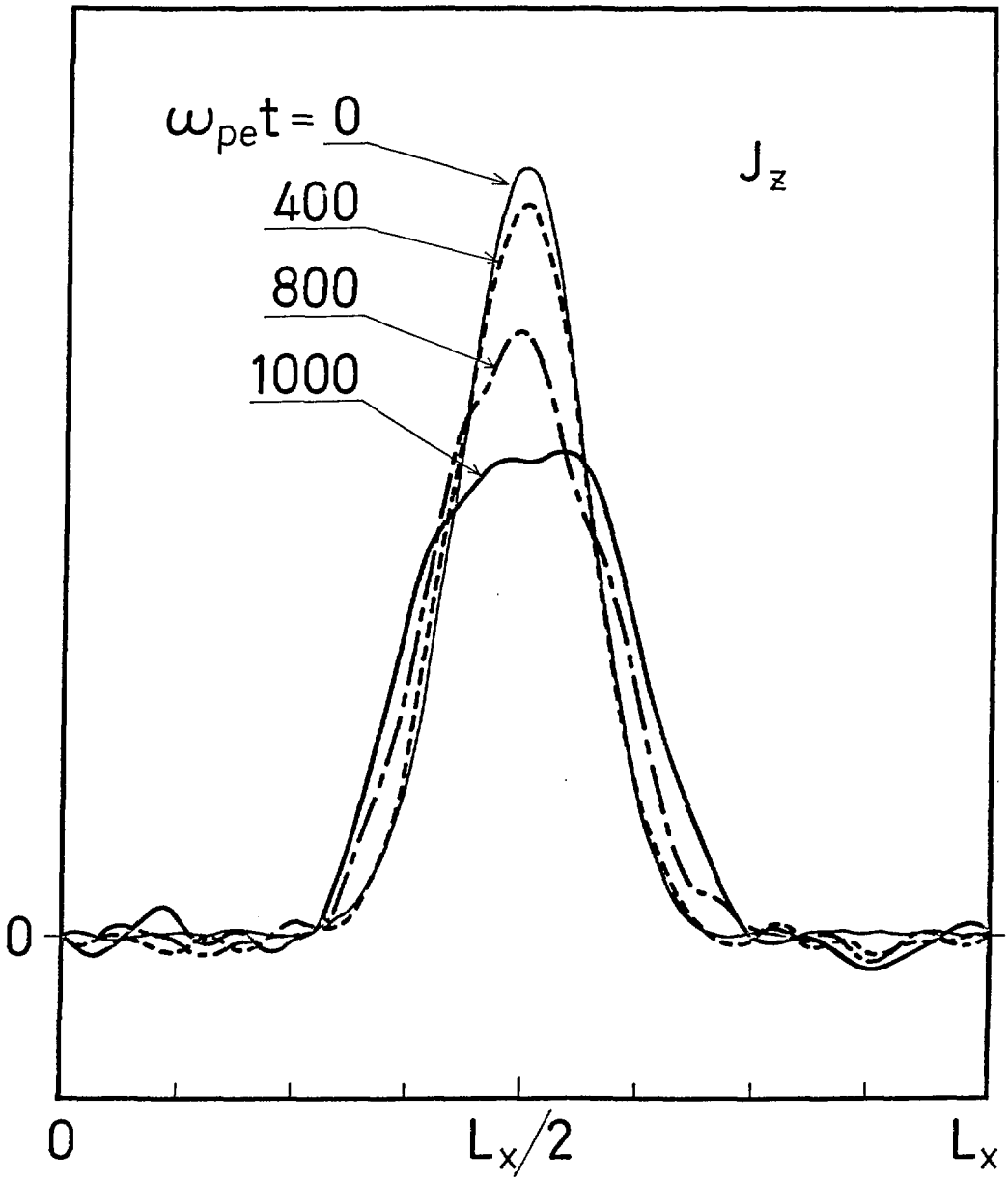

Fig.11

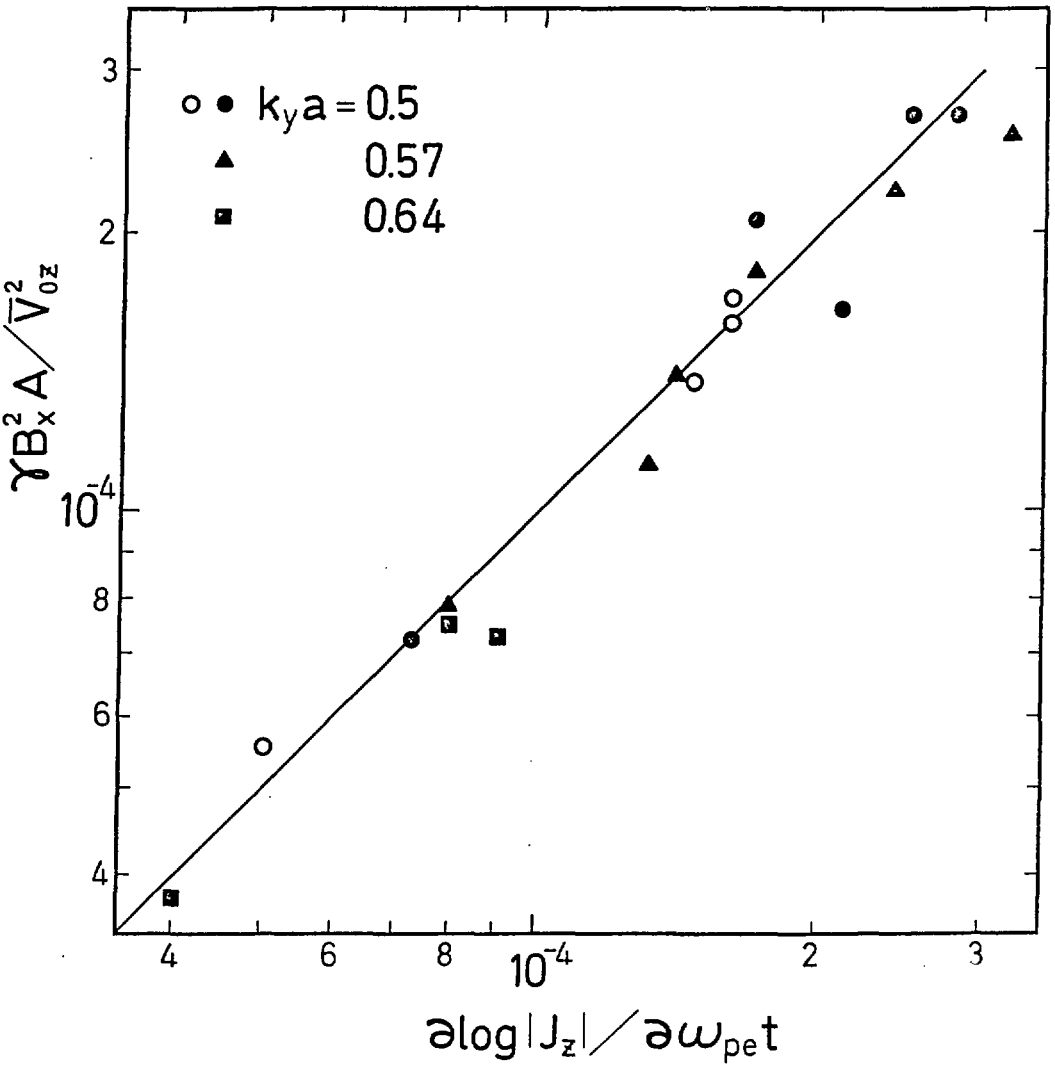
$k_y a = 0.5$
0.57
0.64
$\gamma B_x^2 A / \bar{V}_{0z}^2$
10^{-4}
3
2
8
6
4
$\partial \log |J_z| / \partial \omega_{pe} t$

Fig.12

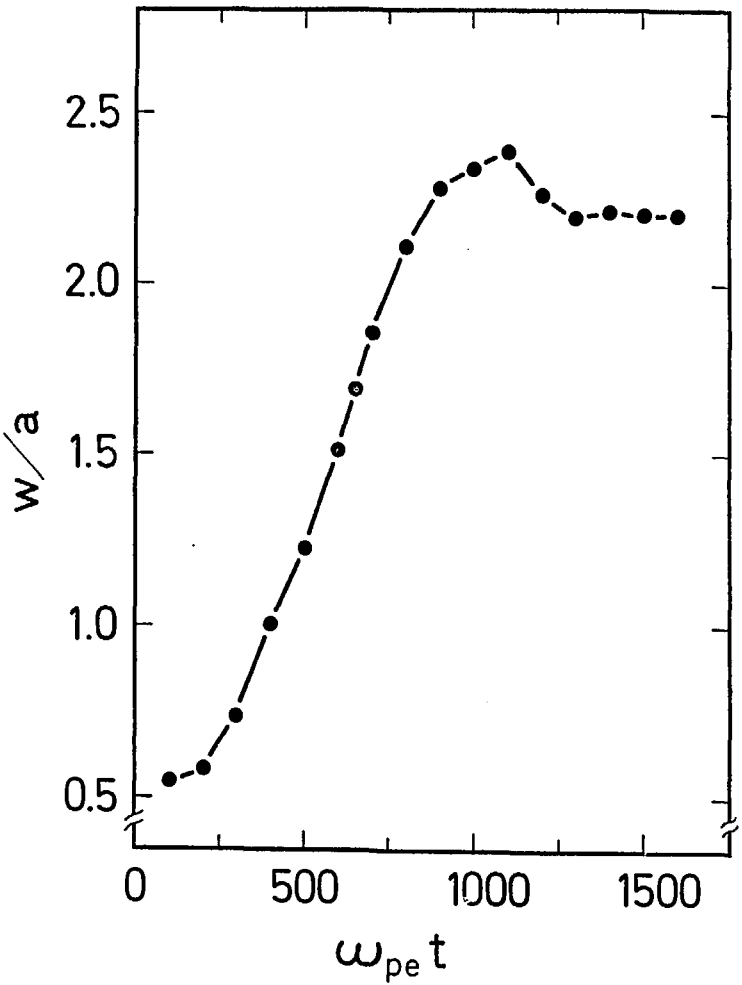
2.5
2.0
1.5
1.0
0.5
w/a
0
500
1000
1500
ωpe t

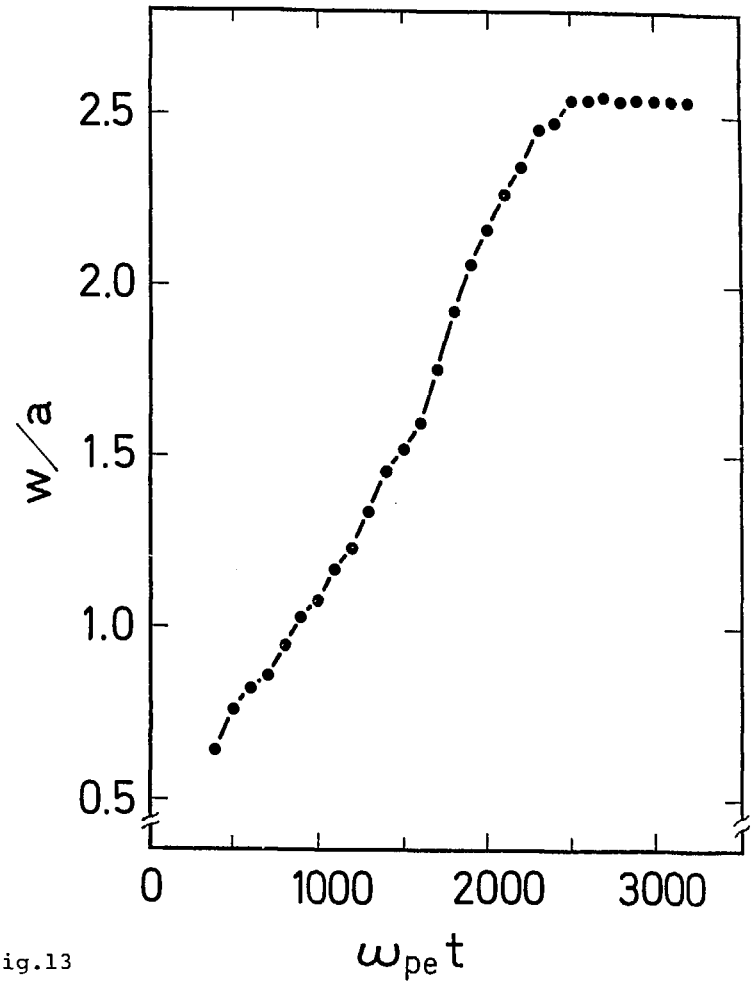
2.5
2.0
1.5
1.0
0.5
w/a
0
1000
2000
3000
ωpe t

Fig.13

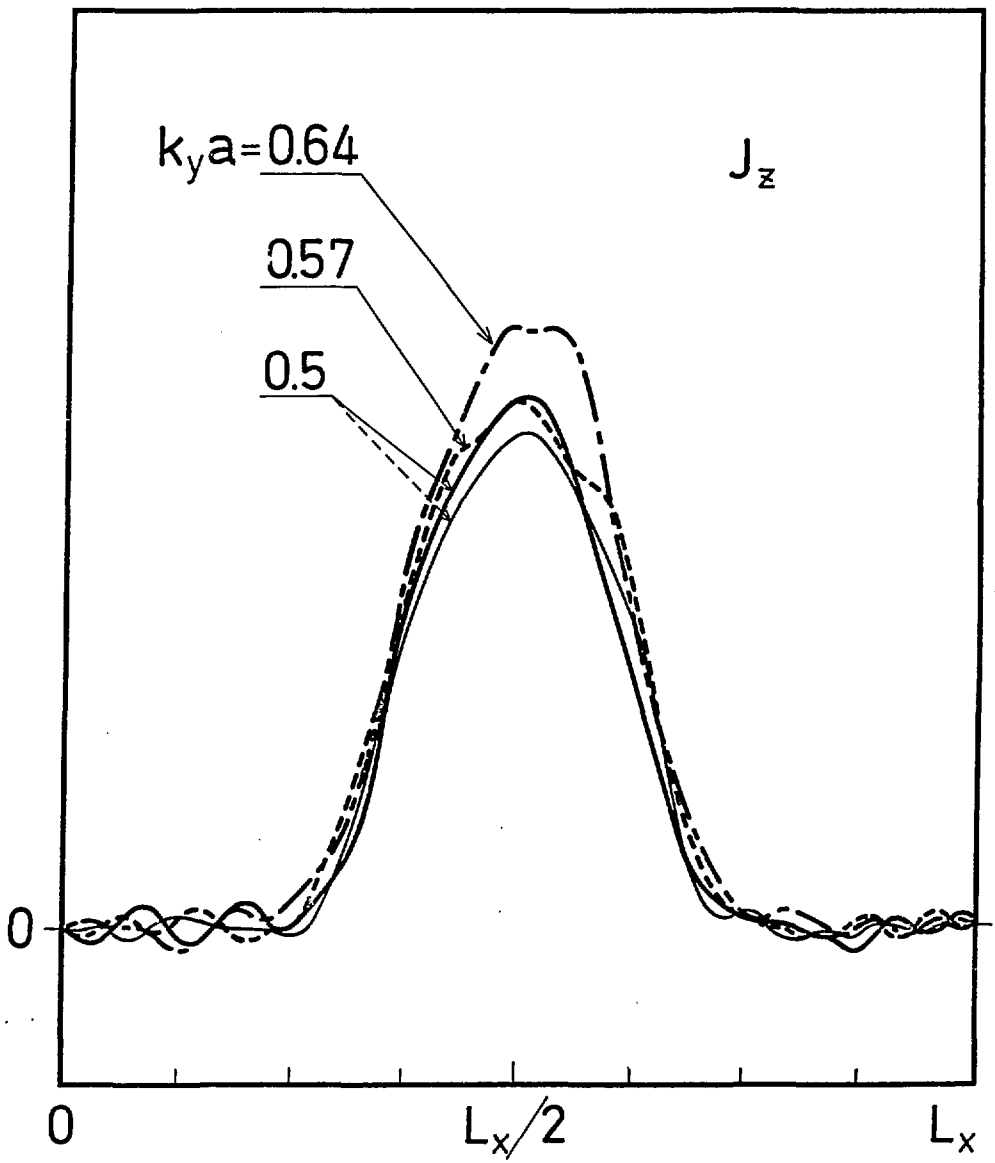

Fig.14

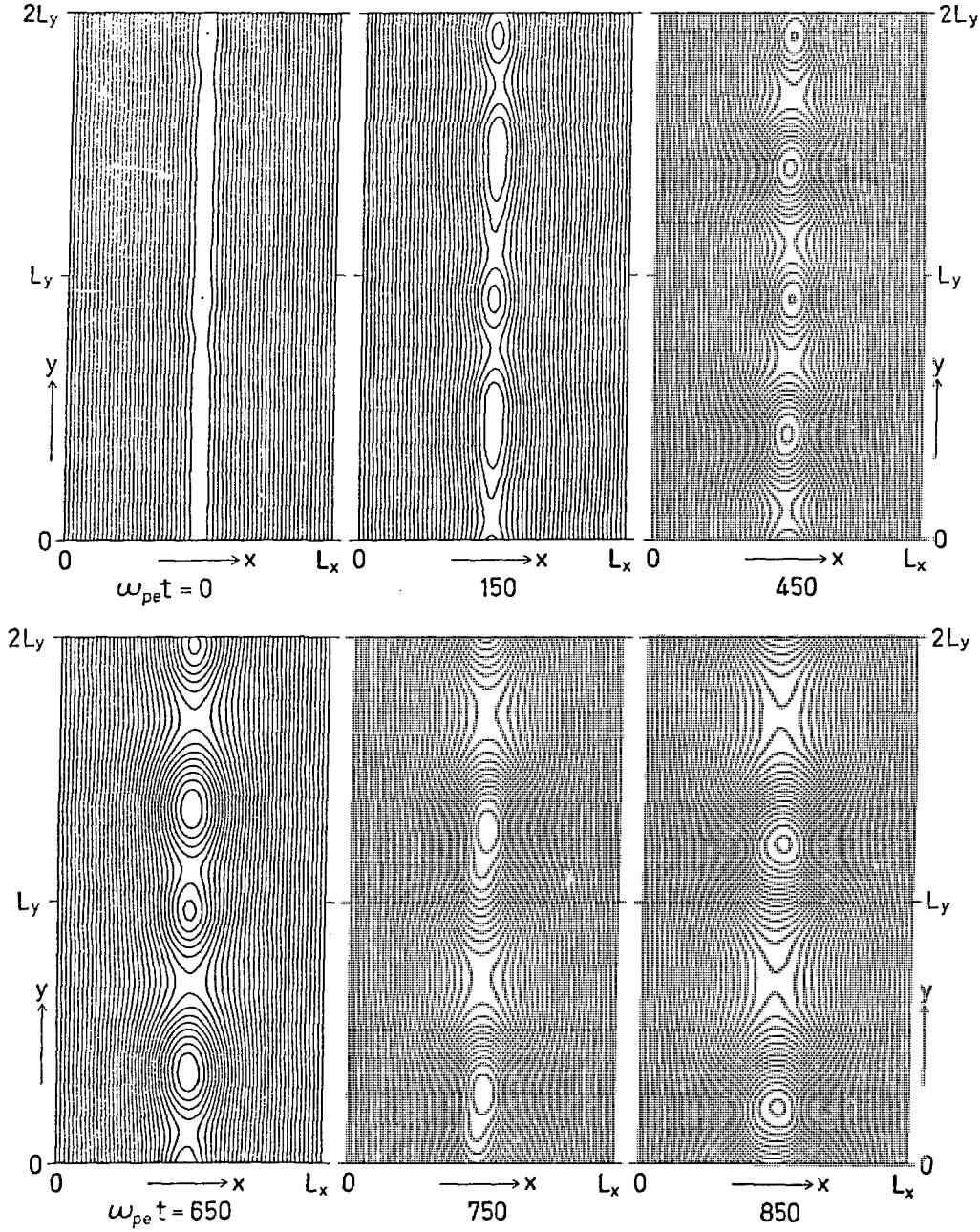

Fig.15

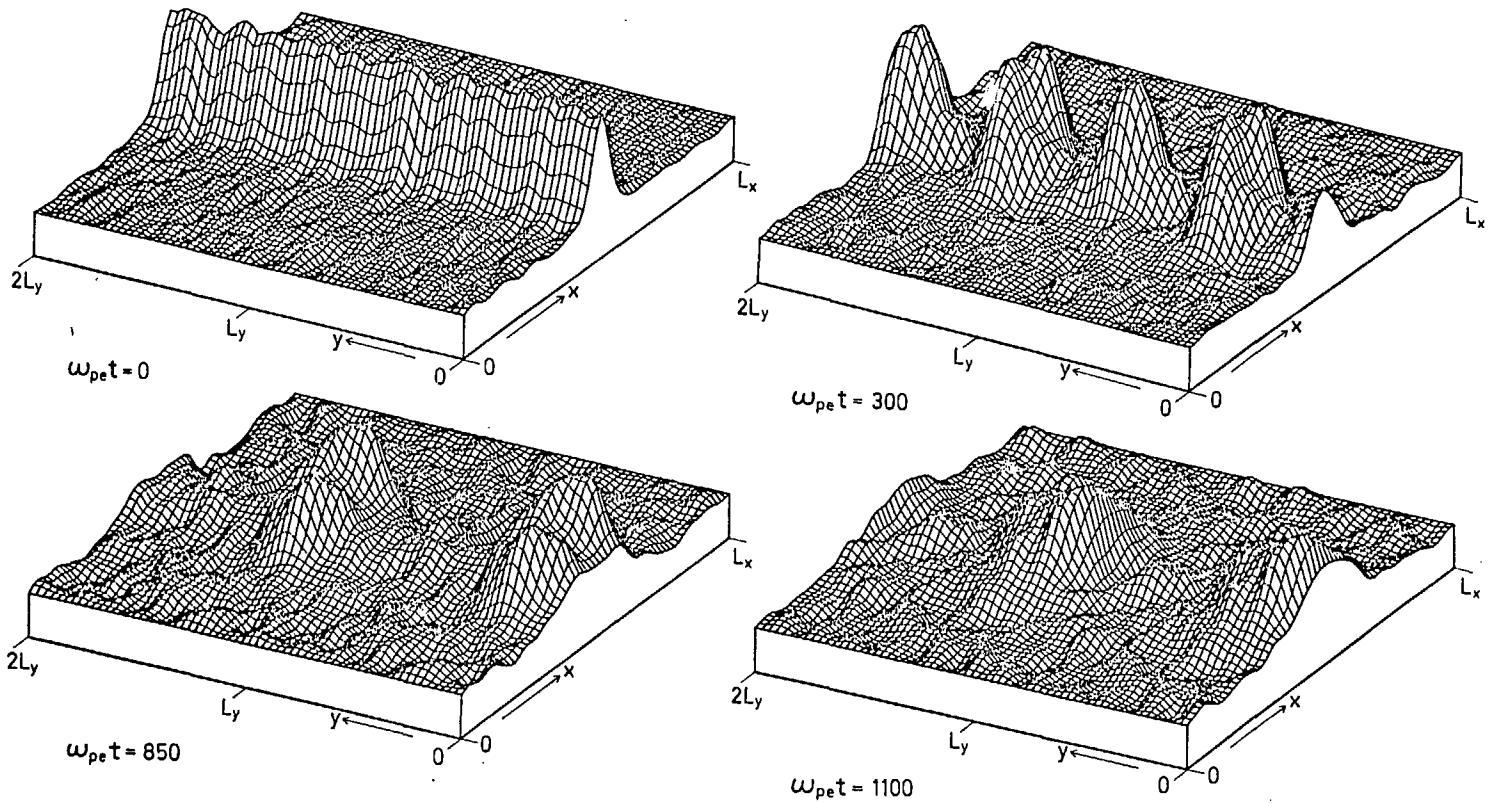
$\omega_{pe}t = 0$
$\omega_{pe}t = 300$
$\omega_{pe}t = 850$
$\omega_{pe}t = 1100$
$2L_y$
L_y
L_x
y
x
0

Fig.16

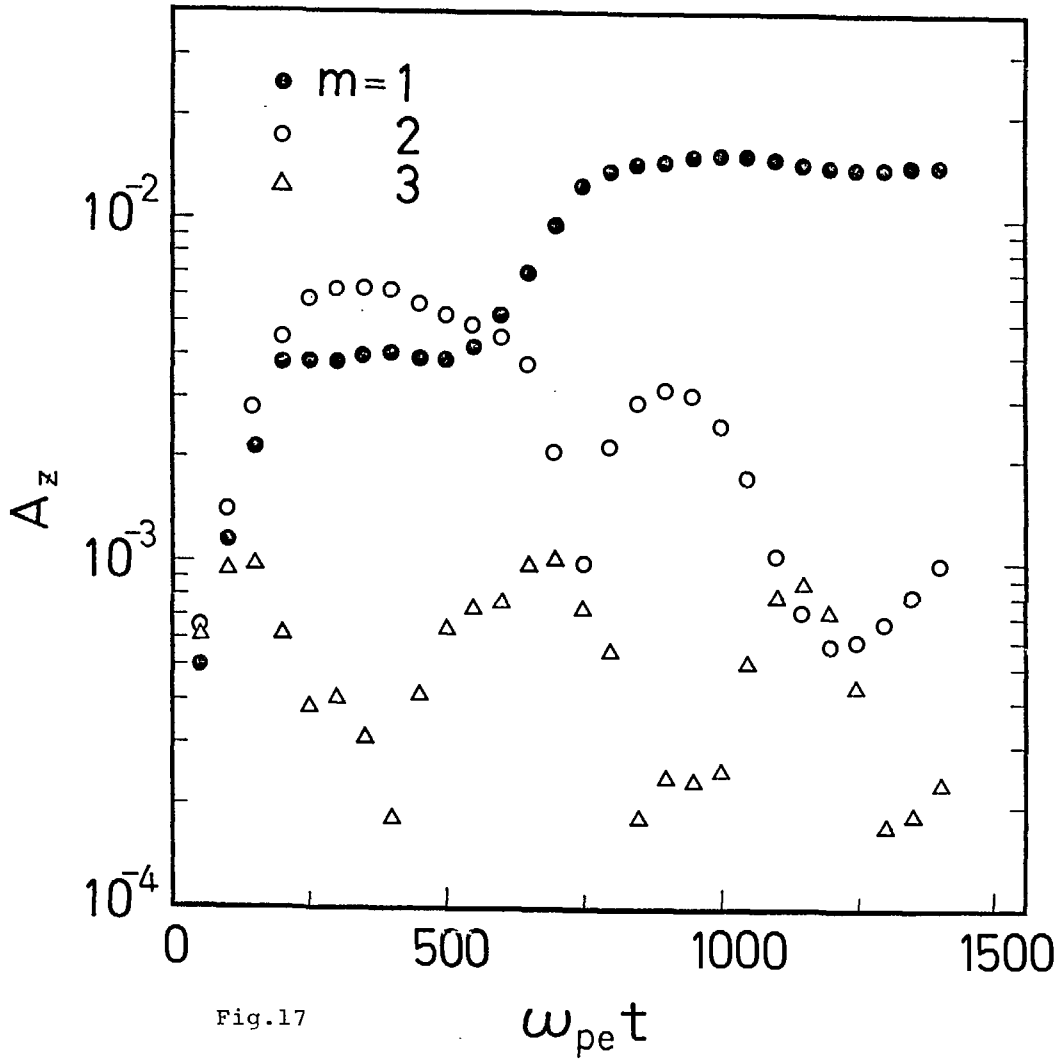

Fig.17